

OPTIMIZATION OF PERFORMANCE PARAMETERS FOR  
LARGE AREA SILICON PHOTOMULTIPLIERS  
FOR USE IN THE GLUEX EXPERIMENT

A THESIS

SUBMITTED TO THE FACULTY OF GRADUATE STUDIES AND RESEARCH  
IN PARTIAL FULFILLMENT OF THE REQUIREMENTS

FOR THE DEGREE OF

MASTER OF SCIENCE

IN PHYSICS

UNIVERSITY OF REGINA

by

Kathryn Louise Janzen

Regina, Saskatchewan

January, 2010

© Copyright 2010: K.L. Janzen

# Abstract

Largely because of their resistance to magnetic fields, silicon photomultipliers (SiPMs) are being considered as the readout for the GlueX Barrel Calorimeter, a key component of the GlueX detector located immediately inside a 2.2 T superconducting solenoid. SiPMs with active area  $1 \times 1 \text{ mm}^2$  have been investigated for use in other experiments, but detectors with larger active areas are required for the GlueX BCAL. This puts the GlueX collaboration in the unique position of being pioneers in the use of this frontend detection revolution by driving the technology for larger area sensors.

SensL, a photonics research and development company in Ireland, has been collaborating with the University of Regina GlueX group to develop prototype large area SiPMs comprising 16 -  $3 \times 3 \text{ mm}^2$  cells assembled in a close-packed matrix.

Performance parameters of individual SensL  $1 \times 1 \text{ mm}^2$  and  $3 \times 3 \text{ mm}^2$  SiPMs along with prototype SensL SiPM arrays are tested, including current versus voltage characteristics, photon detection efficiency, and gain uniformity, in an effort to determine the suitability of these detectors to the GlueX BCAL readout.

# Acknowledgements

This thesis is the culmination of contributions made by many people. Whether it be by providing professional or technical advice, or by taking an interest in this research, the influence on this project by those people has been sincerely appreciated.

To my supervisors, Dr.G.J.Lolos and Dr.Z.Papandreou, I owe an inestimable debt for their guidance, advice and patience. Their professional and academic competence are an inexhaustible source of insight and wisdom, and served as a solid foundation for the development of this work in Regina. I am thankful for the financial support I received through their NSERC grants.

I would like to acknowledge the significant contributions made to this project by Mr.D.Kolybaba and Mr.K.Wolbaum through their technical knowledge and advice, and in the fabrication of experimental apparatuses. Dr.A.Semenov's expertise in both experimental design and analysis techniques have proven to be an invaluable resource throughout this project.

Thanks are due to JLab research scientist, Mr.C.Zorn, and SensL Project Manager, Dr.P.Hughes for their communications which evidenced both vast knowledge of SiPMs, and geniality, lending this project an international perspective.

I gratefully acknowledge both The Faculty of Graduate Studies and Research and NSERC for the financial support received in the form of scholarships.

Finally, I would like to thank my family, friends and fellow students for their support, understanding and encouragement.

For providing love,  
Kindness, wisdom and good genes,  
To Geo and Lyn.

# Contents

<b>Abstract</b>	<b>i</b>
<b>Acknowledgements</b>	<b>ii</b>
<b>Dedication</b>	<b>iii</b>
<b>List of Figures</b>	<b>ix</b>
<b>List of Tables</b>	<b>x</b>
<b>1 Introduction</b>	<b>1</b>
1.1 Outline of Thesis . . . . .	3
<b>2 QCD and Gluonic Excitations</b>	<b>5</b>
2.1 Quantum Chromodynamics . . . . .	5
2.2 Colour Confinement . . . . .	6
2.3 Conventional Hadrons . . . . .	7
2.4 Glueballs and Hybrid Mesons . . . . .	8
2.5 Hybrid Meson Photoproduction . . . . .	12
2.6 Exotic Hybrid Identification . . . . .	13
<b>3 The GlueX Barrel Calorimeter</b>	<b>14</b>
3.1 The GlueX Detector . . . . .	14

3.1.1	Beam Tagger . . . . .	16
3.1.2	Calorimetry . . . . .	17
3.1.3	Charged Particle Tracking . . . . .	18
3.1.4	Particle Identification . . . . .	18
3.2	The GlueX BCAL . . . . .	19
3.2.1	Scintillating Fibres . . . . .	21
3.2.2	Readout Requirements . . . . .	23
3.3	BCAL Readout Options . . . . .	25
<b>4</b>	<b>Silicon Photomultipliers</b>	<b>27</b>
4.1	Avalanche Photodiodes . . . . .	28
4.2	Silicon Photomultipliers . . . . .	30
4.2.1	Cross Talk . . . . .	32
4.2.2	Dark Rate . . . . .	33
4.2.3	Photon Detection Efficiency . . . . .	33
4.2.4	Recovery Time . . . . .	36
4.2.5	Linearity . . . . .	36
4.2.6	Dynamic Range . . . . .	37
4.3	SiPM Arrays . . . . .	39
4.3.1	Gain Uniformity . . . . .	40
4.4	Measurements of Performance . . . . .	41
<b>5</b>	<b>SensL SiPMs in Regina</b>	<b>42</b>
5.1	Introduction . . . . .	42
5.2	SPMMicros . . . . .	44
5.2.1	IV Characterization . . . . .	46
5.2.2	Qualitative Performance Evaluation . . . . .	51

5.2.2.1	Limits in Linearity . . . . .	53
5.2.2.2	Individual Photoelectron Peaks . . . . .	57
5.2.2.3	Cooling Effects . . . . .	57
5.2.3	Photon Detection Efficiency . . . . .	60
5.2.3.1	Description of Experimental Setup . . . . .	60
5.2.3.2	Measurements and Analysis . . . . .	64
5.3	SensL SiPM Arrays . . . . .	73
5.3.1	IV Characterization . . . . .	75
5.3.2	Gain Uniformity . . . . .	76
5.3.3	Signal Analysis . . . . .	89
<b>6</b>	<b>Conclusions</b>	<b>91</b>
	<b>References</b>	<b>94</b>

# List of Figures

1.1	Diagram of projected JLab upgrades. . . . .	2
2.1	Schematic diagram of a meson nonet. . . . .	9
3.1	Side-view schematic of the GlueX detector. . . . .	15
3.2	Views of the GlueX BCAL. . . . .	20
3.3	Diagram of a double-clad optical fibre. . . . .	22
4.1	Typical IV characteristic of an APD. . . . .	29
4.2	SiPM topology schematic. . . . .	31
4.3	Typical spectral response of a SiPM device. . . . .	35
4.4	Response showing linearity of a typical SiPM device. . . . .	38
5.1	Photographs of SensL SPMMicros (and (a) electronic board) tested in Regina (original in colour). . . . .	45
5.2	Typical IV curve of a 3-mm SPMMicro. . . . .	47
5.3	Sample IV characteristics of all SPMMicro types tested in Regina (original in colour). . . . .	49
5.4	A photo of the PicoQuant laser used for SiPM tests in Regina (original in colour). . . . .	52
5.5	Sample scope traces from a SPMMicro device showing electronic saturation. . . . .	54



5.6	Scope traces and ADC spectra showing a baseline offset in SPMMicro signals at high laser pulse frequency resulting in an ADC shift. . . . .	55
5.7	Sample SPMMicro ADC spectra taken at room temperature. . . . .	58
5.8	Cooling results for 3-mm A35HD SPMMicro devices . . . . .	59
5.9	Typical signal and corresponding ADC spectrum showing individual photoelectron peaks detected by a 3-mm A35HD SPMMicro at -20°C with laser intensity 2.60. . . . .	61
5.10	Views of the experimental setup for SPMMicro PDE tests. . . . .	63
5.11	The quantum efficiency of a calibrated photodiode compared to the emission spectrum of a scintillating fibre. . . . .	65
5.12	Sample ADC spectra for 3-mm A20HD-07 SPMMicro at (a) low laser intensity where individual peaks are visible, and (b) high laser intensity where peaks are not visible. . . . .	67
5.13	SPMMicro 3-mm A20HD PDE at overbias +3.0 V, gate duration 160 ns and laser frequency 2.5 MHz. . . . .	69
5.14	SPMMicro 3-mm A20HD-07 PDE at (a) overbiases of +2.0 V, +2.5 V and +3.0 V, laser frequency 2.5 MHz, and ADC gate width 120 ns, and (b) ADC gate widths of 120 ns and 160 ns, laser frequency 2.5 MHz, and overbias +3.0 V. . . . .	70
5.15	Measured PDE values for 1-mm A20HD and A35HD and 3-mm A20HD SPMMicros. . . . .	72
5.16	Photographs of SensL SiPM arrays that were tested in Regina (original in colour). . . . .	74
5.17	IV characteristics of SensL SiPM arrays (original in colour). . . . .	77
5.18	An image of a glass-mounted array illustrating the orientation of the x- and y-axes on the array (original in colour). . . . .	79

5.19	Amplitude ratio measurement of the first SensL glass-mounted array (original in colour). . . . .	80
5.20	(a) Picture of the experimental apparatus built in Regina for gain uniformity testing of G-series glass-mounted arrays (original in colour), along with (b) a cross-sectional sketch of a single hole in the apparatus.	82
5.21	The average amplitude ratios for G-series glass-mounted arrays (origi- nal in colour). . . . .	82
5.22	Pictures of the experimental apparatus built in Regina for gain unifor- mity testing of SensL SPMPlus and SPMPs (original in colour). . . .	84
5.23	The average amplitude ratios for individual cells of the first SensL SPMPlus (original in colour). . . . .	84
5.24	The amplitude ratio results of surface scans of each individual cell in the SPMPlus array (original in colour). . . . .	86
5.25	The average amplitude ratios for SPMP arrays (original in colour). . .	87
5.26	Typical signal produced from the SensL SPMPlus . . . . .	88
5.27	Typical signals produced from the SensL SPMP arrays . . . . .	90

# List of Tables

2.1	A list of the eight nonets of hybrid mesons. . . . .	11
5.1	Characteristics of SensL SPMMicro devices. . . . .	50
5.2	PDE values for SPMMicros as determined in Regina. . . . .	72
5.3	SiPM array breakdown voltages as determined in Regina. . . . .	77

# Chapter 1

## Introduction



ear the edge of the Virginia Peninsula on the east coast of the United States, sits the Thomas Jefferson National Accelerator Facility (JLab), a laboratory committed to exploring the nature of matter and how the world fits together. Through the years, researchers in three experimental halls (Halls A, B, and C) have made use of the 6 GeV electron beam produced at JLab to make great scientific advances, but now new physics is being pursued and adjustments must be made in the experimental facilities. In April 2009, ground was broken for a fourth experimental hall (Hall D). This, along with other upgrades, including a new beamline and increased refrigeration capacity (see Figure 1.1), will give the flourishing facility the ability to deliver a 12 GeV electron beam to Hall D, thus further expanding its scientific reaches. Driving the upgrade is an experiment called GlueX (named for its search for *gluonic excitations*) which, since 1997, has quietly developed into an international collaboration involving over 60 researchers at 15 institutions around the world.

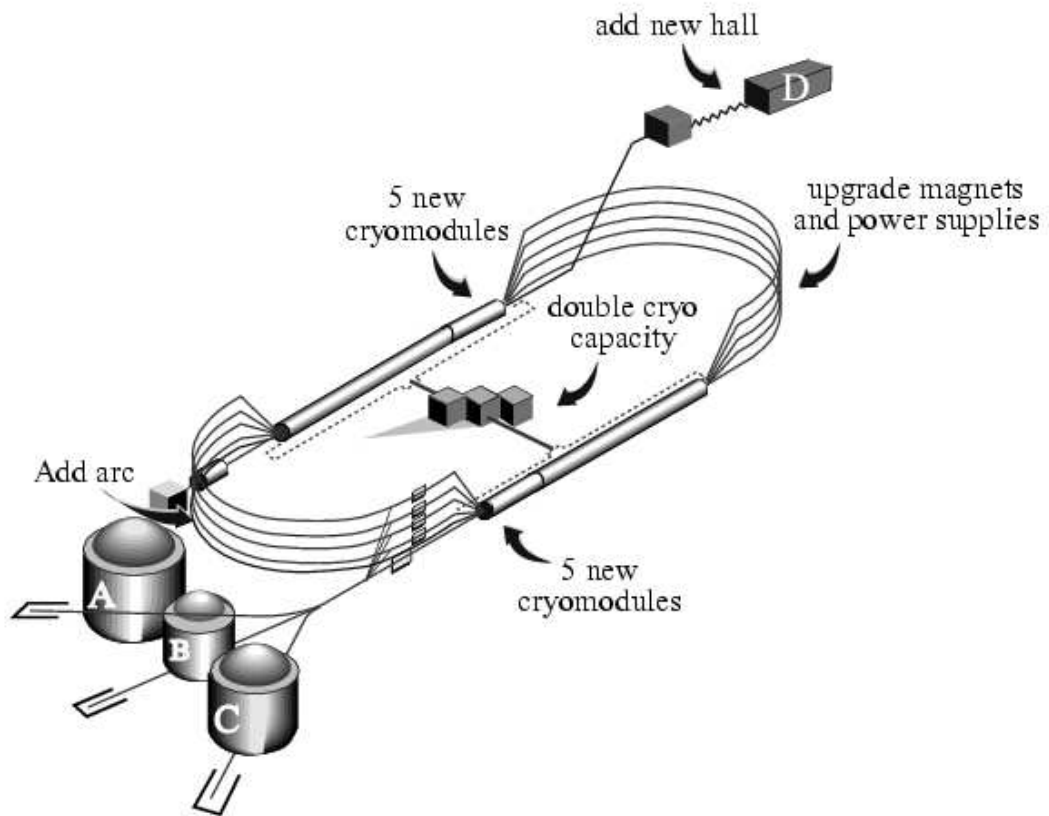


Figure 1.1: Diagram of projected JLab upgrades including beamline additions, increased cooling capacity and a new experimental hall.

## 1.1 Outline of Thesis

The purpose of this thesis is to discuss large area silicon photomultipliers (SiPMs) in the context of the GlueX experiment. Because of their immunity to large magnetic fields, SiPMs not only have considerable applications in medical diagnostic tools such as Positron Emission Topography (PET) and Magnetic Resonance Imaging (MRI), but are also ideal for use in particle physics experiments. While SiPMs up to  $3 \times 3 \text{ mm}^2$  in area have already been developed and studied, the GlueX collaboration proposes the assembly of 16 -  $3 \times 3 \text{ mm}^2$  SiPM elements into a close-packed matrix as the read-out for the barrel calorimeter (BCAL), a subsystem of the GlueX detector designed to detect photons. Since large array SiPM arrays have not been used in large experiments before, a significant amount of research and development was necessary to finally obtain devices capable of meeting the specifications of GlueX. This thesis outlines the Regina group's contribution to research and development efforts.

To provide the framework of this project, a synopsis of the physics motivation behind the GlueX experiment is given in Chapter 2, beginning with a basic overview of Quantum Chromodynamics (QCD) and the strong force. Particular emphasis is placed on the importance of mapping out the exotic hybrid meson spectrum in order to better understand gluonic excitations and confinement - the goal of GlueX. Other experimental groups such as the Crystal Barrel (CBAR) and E852 collaborations have provided tantalizing evidence of gluonic excitations, but more convincing data are needed to address the confinement of quarks and gluons. GlueX plans to map out the entire spectrum of gluonic excitations in their nonets, providing a quantitative understanding of confinement.

In order to achieve the physics goals of GlueX, a detector capable of measuring the four-momenta of both charged particles and photons must first be in place. The GlueX collaboration has designed a hermetic detector system comprising several

subsystems. Regina's main contribution is the BCAL, a cylindrical electromagnetic calorimeter which will measure the four-momenta of photons resulting from the decays of photoproduced mesons. In Chapter 3, an overview of the GlueX detector is given along with a more detailed description of the BCAL and its position within the greater detector. This leads into a discussion of the readout for the BCAL, where the benefits of SiPMs (as opposed to photomultiplier tubes (PMTs)) are outlined.

SiPMs are described in Chapter 4 beginning with a characterization of basic avalanche photodiodes and leading into a description of large area SiPM arrays. This includes a discussion of important design features and performance parameters of SiPM arrays.

In Chapter 5, the specific devices tested at the University of Regina are introduced and measurements of performance parameters of SiPMs are presented. The set of devices tested in Regina comprise  $1 \times 1 \text{ mm}^2$  and  $3 \times 3 \text{ mm}^2$  SiPMs and  $4 \times 4 - 3 \times 3 \text{ mm}^2$  SiPM arrays, and the measurements taken include current versus voltage characteristics, photon detection efficiencies, gain uniformities and a qualitative account of single photoelectron capabilities for various detectors. The experimental methods used for each measurement are laid out along with specific results.

A discussion of those results and their implications within the GlueX experiment are presented in Chapter 6.

## Chapter 2

# QCD and Gluonic Excitations

### 2.1 Quantum Chromodynamics



our fundamental forces of nature dictate how all matter behaves and interacts throughout the Universe. These are the gravitational, electromagnetic, weak, and strong forces. Each interacts with certain particles, but not with others. For instance, gravity acts between any two massive particles, while the electromagnetic force only interacts with electrically charged particles. Similar to this, the strong interaction (which is, fittingly, the strongest of the four) interacts only between *hadrons* (derived from the Greek  $\alpha\delta\rho\varsigma$ , meaning “strong”), and just as the electromagnetic force is mediated by the photon (a force-carrying particle or *boson*), the strong force is carried by another boson, the gluon. The theory of the strong interaction is called Quantum Chromodynamics (QCD), which follows the same general prescription as Quantum Electrodynamics (QED), but with added peculiarities.

One feature which distinguishes QCD from QED relates to the way particles behave in the strong interaction at a distance. At short distances (say, less than the size of a hadron), the “strong” potential is very weak, while at greater distances, the potential is indeed strong and increases linearly with distance. This effectively



means that at the former scale, quarks are only weakly bound and exhibit properties similar to those of free particles (called *asymptotic freedom*), and at the latter scale, it is impossible to physically separate quarks from each other (called *confinement*). This phenomenon adds complexity to any investigation of the strong interaction, and can be explained by an important characteristic of gluons.

## 2.2 Colour Confinement

At first glance, the attraction between quarks appears not unlike that of electrically charged particles. The role of electric charge in QED is played by *colour* charge in QCD, and the two interactions are each mediated by an exchange of bosons (gluons and photons respectively); however, there is an important difference. While photons are electrically neutral, gluons themselves carry colour charge. As an electron and a proton are pulled apart, their attraction to one another decreases as distance increases. This is not the case with the strong force.

According to the Flux Tube Model [1], gluon fields form colour-charged flux tubes which bind quarks together. As a quark and an antiquark are pulled apart, those flux tubes stretch, similar to rubber bands, drawing the quark-antiquark pair back together. The force of attraction between the two quarks (and the colour-charged gluonic flux tube) remains constant (although the potential increases linearly with distance) regardless of the distance between them. If they continue to be pulled apart, at some point the energy injected into the system rises above the energy required to spontaneously produce a new quark and antiquark which, once produced, couple with the original antiquark and quark respectively to create two new pairs where there once was one. The idea of gluonic colour charge opens up the world of unconventional hadrons, but before the rich world of exotic particles is explored, a description of conventional hadrons is needed.

## 2.3 Conventional Hadrons

Hadrons are particles made up of quarks and antiquarks held together by gluonic flux tubes mediating the strong force. In the Standard Model, there are six *flavours* of quark (up, down, charm, strange, top and bottom) and six corresponding flavours of antiquark. These are often broken down into two groups: light quarks (u, d and s) and heavy quarks (c, b and t). Along with a fractional electric charge (up, charm and top quarks carry  $+\frac{2}{3}e$ ; down, strange and bottom quarks carry  $-\frac{1}{3}e$ ), each quark is believed to carry colour charge (either red, blue, or green), with each antiquark carrying an anticolour charge. Gluons carry colour charge in the form of some colour-anticolour combination.

While the introduction of colour charge provides a convenient analogy to electric charge, no colour-charged particle has ever been observed. The Quark Model [2] suggests that the strong force causes quarks to bind together into hadrons which are all *colourless* particles, or colour *singlets*. Among hadrons, baryons are composed of three quarks, each with a different colour charge ( $qqq$ ), and mesons, the simplest hadrons, are made up of one quark with a certain colour charge and one antiquark with the corresponding anticolour charge ( $q\bar{q}$ ).

The picture of a meson as a quark-antiquark pair stuck together by gluons and sitting isolated in nothingness may be overly simplistic. More probably, mesons consist of a valence quark and valence antiquark arising from a sea of gluons and virtual quarks of all flavours and colour-charges. Although this rich assortment of virtual particles exists, it is only the valence quark-antiquark pair (bound by a gluonic flux tube) that can be observed and which contributes to the characteristics and quantum numbers associated with a certain meson.

Hundreds of mesons have been observed and identified over the years, which means physicists need a classification system akin to the Periodic Table of elements in Chem-

istry. As it turns out, mesons can be categorized into groups of nine such that each *nonet* is characterized by unique values of  $J^{PC}$ , where  $\vec{J}$  denotes total angular momentum, and  $P$  and  $C$  refer to parity and charge conjugation respectively (see Figure 2.1). For mesons,  $\vec{J}$  depends on the total spin  $\vec{S}$  of the two quarks, which each have spin- $\frac{1}{2}$ , as well as the total orbital angular momentum,  $\vec{L}$ . Mathematically,  $\vec{J} = \vec{L} + \vec{S}$ . The two quark spins can only be parallel ( $\vec{S} = 1$ ) or anti-parallel ( $\vec{S} = 0$ ). Parity and charge conjugation quantum numbers describe certain symmetries. If a meson is symmetric through spatial inversion,  $P$  is assigned a plus symbol, and if it is symmetric through particle-antiparticle interchange,  $C$  is assigned a plus symbol. If a meson is antisymmetric under either of these conditions, then the corresponding quantum number is a minus sign. Mathematically, these conditions are expressed as  $P = (-1)^{L+1}$  and  $C = (-1)^{L+S}$ . Thus, assuming that all contributions to these quantum numbers come from the quark and antiquark in the system, only certain  $J^{PC}$  combinations are allowed. For instance, for mesons where  $\vec{S}$  and  $\vec{L}$  can each take values of 0 or 1, there are only six allowed  $J^{PC}$  combinations:  $\{0^{-+}, 0^{++}, 1^{--}, 1^{+-}, 1^{++}, 2^{++}\}$ .

Part of the beauty of the meson nonet classification system is that it not only classifies each meson as belonging to a certain nonet, but it also predicts the existence of new mesons in incomplete nonets. As soon as one meson with a certain  $J^{PC}$  has been observed, based on the symmetry of the nonets, the existence of eight more mesons with that same  $J^{PC}$  combination is automatically implied.

## 2.4 Glueballs and Hybrid Mesons

As aforementioned, the idea of gluons carrying colour charge has important implications. If gluons carry colour charge, they must be able to bind together (self interaction) to form a colour singlet hadron. This would result in a *gluonic* meson made up entirely of gluons called a *glueball*. Experiments such as WA102 and Crystal Barrel

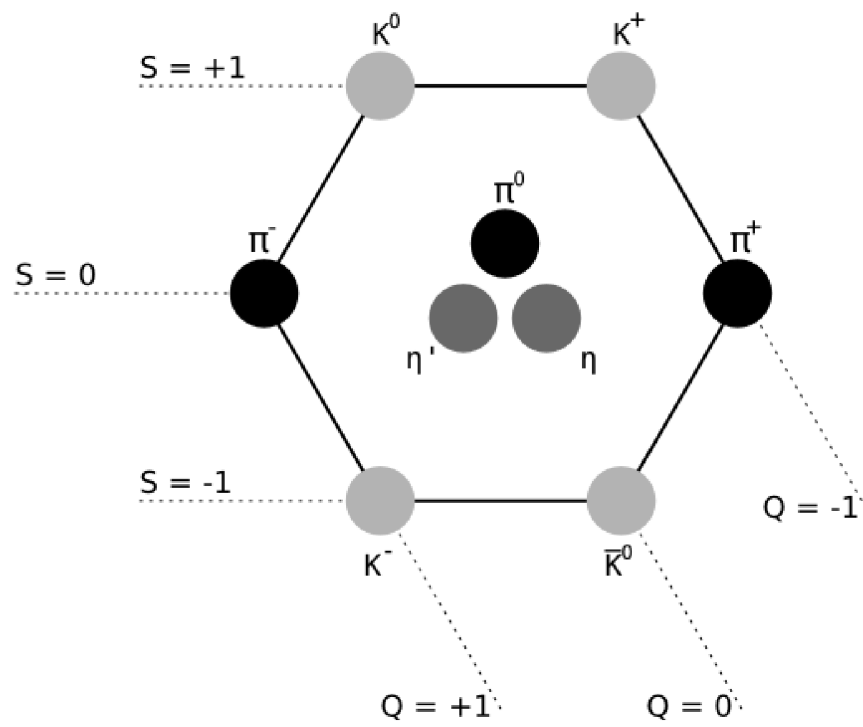


Figure 2.1: Schematic diagram of a meson nonet. In this case,  $J^{PC} = 0^{-+}$ .

have searched for light glueballs with a mass of about  $1.6 \text{ GeV}/c^2$ , but so far all evidence of gluonic mesons has been shrouded by the *mixing* of glueballs with conventional mesons [3]. Particles are experimentally identified based on their quantum numbers and decay modes, but as multiple particles can share these characteristics, mixing implies that each observed particle is a linear superposition of mass eigenstates of all particles that share specific quantum numbers and decay modes. Since these light glueballs share  $J^{PC}$  values with conventional mesons, they are difficult to identify with certainty despite experimental evidence suggesting an overpopulation of certain states (which could be attributed to the presence of glueballs). To obtain unambiguous evidence of gluonic excitations, other types of unconventional particles must be studied.

The discussion of mesons has heretofore included an inherent assumption that gluonic flux tubes connecting quark-antiquark pairs are in a ground state and therefore make no contributions to the quantum numbers of mesons. This is not always the case as, in the Flux Tube Model, the flux tubes can become excited resulting in *hybrid* mesons. Alternatively, this can be thought of as a quark-antiquark pair with a valence gluon ( $q\bar{q}g$ ). The first excited transverse mode of the flux tube corresponds to a rotation (either clockwise or anticlockwise) about the axis joining the quark-antiquark pair, fixed in space and with  $J = 1$ . Hybrid mesons have a distinct advantage over glueballs for detection in that they exhibit both quark and gluonic degrees of freedom. This means  $J^{PC}$  combinations which were previously thought to be forbidden are actually quite possible. In fact, there are eight predicted nonets of hybrid mesons (see Table 2.1) and, of those eight, three have conventionally forbidden (or *exotic*)  $J^{PC}$  combinations, which means they can be unambiguously detected without any risk of mixing with conventional mesons. According to lattice gauge calculations, the lightest of the exotic hybrid mesons will have a mass of about  $1.8 \text{ GeV}/c^2$ . To fully

Table 2.1: A list of the eight nonets of hybrid mesons. Three of the hybrids with  $S = 1$  (spins aligned) have conventionally forbidden  $J^{PC}$  values.

$J_g$	$S_{q\bar{q}}$	$J^{PC}$	Type	Sample Members
1	0	$1^{++}$	normal	$a_1, f_1, f'_1$
1	0	$1^{--}$	normal	$\rho_1, \omega_1, \phi_1$
1	1	$0^{-+}$	normal	$\pi_0, \eta_0, \eta'_0$
1	1	$0^{+-}$	exotic	$b_0, h_0, h'_0$
1	1	$1^{-+}$	exotic	$\pi_1, \eta_1, \eta'_1$
1	1	$1^{+-}$	normal	$b_1, h_1, h'_1$
1	1	$2^{-+}$	normal	$\pi_2, \eta_2, \eta'_2$
1	1	$2^{+-}$	exotic	$b_2, h_2, h'_2$

map out the exotic hybrid spectrum, a mass reach of up to  $2.8 \text{ GeV}/c^2$  is required.

These exotic hybrid mesons are the primary target of the GlueX experiment on its mission to map out the exotic hybrid meson spectrum, thus furthering our knowledge of the strong interaction and confinement [4–8].

## 2.5 Hybrid Meson Photoproduction

In meson spectroscopy, typically pion ( $\pi$ ), kaon ( $K$ ) or photon ( $\gamma$ ) probes are used with a target nucleon to produce mesons. Both  $\pi$  and  $K$  mesons have quark spins anti-aligned ( $S = 0$ ) and  $J^{PC} = 0^{-+}$ . When looking at hybrid mesons, this is combined with  $J = 1$  from the excited flux tube resulting in a total  $J^{PC}$  of either  $1^{++}$  or  $1^{--}$ , which, unfortunately, are non-exotic. A photon probe can also be used to produce mesons, according to the Vector Meson Dominance Model [9]. Photons carry  $J^{PC} = 1^{--}$ , but so do the  $\rho$ ,  $\omega$  and  $\phi$  mesons. Since an observed particle (even a photon) is a superposition of mass eigenstates, there is a certain probability of  $\rho$ ,  $\omega$  and  $\phi$  mesons to be present in the photon beam. It is these *virtual* mesons which allow a hadronic interaction to occur with a target nucleus. The advantage of using a photon probe is that the two virtual quarks (acting as a virtual meson), which are used to produce hybrid mesons, have their spins aligned ( $S = 1$ ). In this case, resulting hybrid mesons are predicted to have six possible  $J^{PC}$  values, three of which are exotic (see Table 2.1) and will provide the sought-after *smoking gun signature* of gluonic excitations that is of great interest to GlueX.

In the photoproduction of hybrid mesons within the desired mass range of the GlueX experiment ( $1.5 \text{ GeV}/c^2$  to  $3.0 \text{ GeV}/c^2$ , accounting for an uncertainty of about  $0.2 \text{ GeV}/c^2$ ), a beam of 9 GeV photons is ideal. At JLab, this photon beam will be produced with an electron beam incident on a  $20 \text{ }\mu\text{m}$  diamond target acting as the radiator, creating a coherent bremsstrahlung. To achieve a 9 GeV photon beam in

this way, a 12 GeV electron beam must first be produced. This necessity has provided much of the drive to upgrade JLab's electron linear accelerator from 6 GeV to 12 GeV.

## 2.6 Exotic Hybrid Identification

Once hybrid mesons have been produced, the problem of identifying them is complicated in that they are too short-lived to be directly detected. Generally, when a photon interacts with a target proton, this produces a proton or neutron along with mesons (both conventional and hybrid). The mesons then further decay, eventually reaching a final state which can be directly detected. With knowledge of only initial and final states, the intermediate states (where exotic hybrid mesons may be found) must be reconstructed. For instance, one possible reaction is

$$\gamma p \rightarrow p\pi^+\pi^-4\gamma,$$

but the complete reaction could take a number of forms [10], including

$$\gamma p \rightarrow p\eta_1 \rightarrow pa_1^-\pi^+ \rightarrow p\rho^-\pi^0\pi^+ \rightarrow p\pi^-\pi^0\pi^0\pi^+ \rightarrow p\pi^+\pi^-4\gamma \text{ or}$$

$$\gamma p \rightarrow p\pi_1^0 \rightarrow pa_1^0\eta \rightarrow p\rho^+\pi^-2\gamma \rightarrow p\pi^+\pi^0\pi^-2\gamma \rightarrow p\pi^+\pi^-4\gamma.$$

Once the final state of an event has been determined, Partial Wave Analysis (PWA) can be used to work backwards through the reaction to identify intermediate particles. Since decays in the strong interaction are governed by conservation of parity, C-parity and isospin, reliable information about intermediate exotic hybrids can be obtained from precise measurements of final states gathered using a hermetic detector system with good resolution. The added complexity of disentangling many possible decay paths which each result in the same final state also allows cross-checking of the PWA methods used. The GlueX detector has been carefully designed to provide precise final state measurements in an effort to finally identify exotic hybrids with certainty.



## Chapter 3

# The GlueX Barrel Calorimeter

### 3.1 The GlueX Detector



In order to achieve its physics goals, the GlueX collaboration has designed a detector system with nearly hermetic ( $4\pi$ ) coverage involving many individual subsystems (see Figure 3.1) [11–13]. The completed detector must be able to measure the four-momenta of all charged particles and photons. This requires that three general issues be addressed: *calorimetry* (measuring energies of charged particles and photons), *tracking* (determining momenta of charged particles) and *particle identification* (identifying final states). In the GlueX detector, two calorimeters (the Barrel Calorimeter (BCAL) and the Forward Calorimeter (FCAL)), two drift chambers (the Central Drift Chamber (CDC) and the Forward Drift Chamber (FDC)), a Time-of-Flight (TOF) wall, and a start counter, along with a 2.2 T superconducting solenoid magnet (originally built at SLAC National Accelerator Laboratory to be used in other experiments, and refurbished in recent years at Indiana University) will be integrated to provide the required measurements. Each individual component must have a uniform response with well-understood acceptance, and excellent resolution. Because PWA will be used to identify photoproduced mesons based

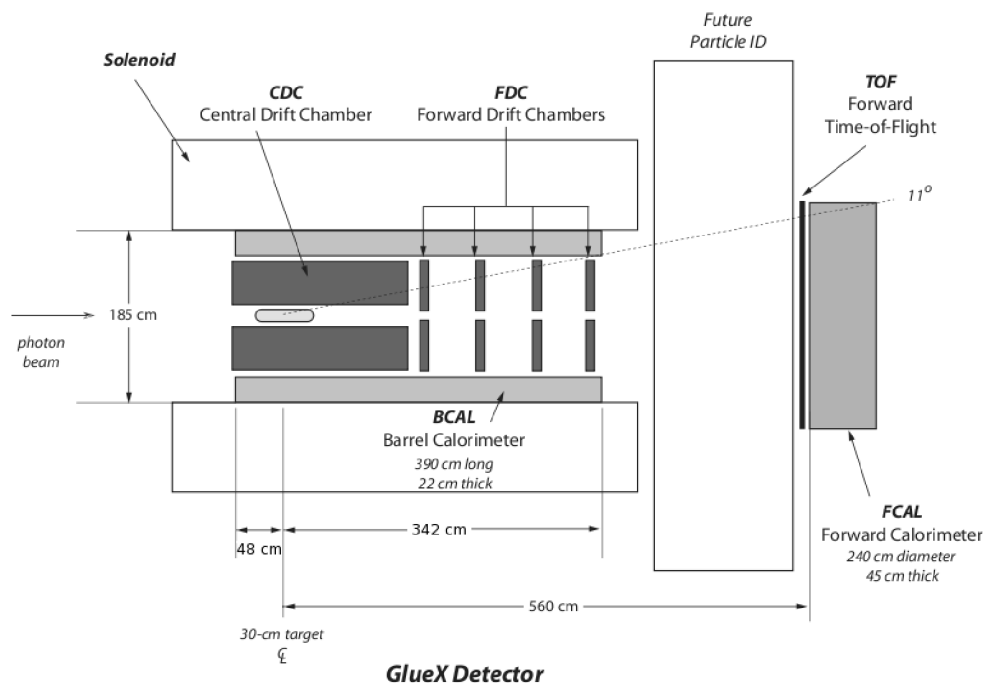


Figure 3.1: Side-view schematic diagram showing the major components of the GlueX detector. The start counter is omitted from the diagram for clarity.

on their decays into other particles, high-statistics data are required, and sensitivity to many final states is essential. After years of careful planning, each of the GlueX detector components is being completed and tested by different groups of researchers. With JLab upgrades also underway to ensure the delivery of the required 9 GeV photon beam to Hall D, commissioning of the detector is expected in 2014. What follows is a brief outline of the GlueX detector and the components it encompasses.

### 3.1.1 Beam Tagger

As JLab's 12 GeV electron beam enters the Photon Source and Tagger building, it is directed by steering magnets towards a crystal radiator mount which houses a thin diamond target used to produce photons. When the electron beam passes through the diamond wafer, bremsstrahlung photons are produced. The diamond wafer can be oriented to provide photon beams of varying energy and polarization. For the GlueX experiment, approximately 40% of the photons will be linearly polarized, and the desired energy range of the photon beam is between 8 and 9 GeV. These photons carry on to the experimental hall while the electrons exiting the target (after producing bremsstrahlung photons) are directed into the tagger spectrometer. There, the electrons' energies and momenta are measured (or *tagged*), providing the energy of the photon associated with the tagged electron, before they are collected in the electron beam dump. As the photon beam makes its way towards the GlueX detector, it passes through a series of sweeping magnets and collimators over a distance of about 70 m. The sweeping magnets remove any electrons generated by photons interacting with material, and the collimators remove the fringes of the beam and preserve the well-polarized beam core. In effect, this process increases the linear polarization of the beam significantly. It is this final optimized beam which will be used, incident on a liquid hydrogen target, to produce mesons for the GlueX experiment. The final

states resulting from decays of those photoproduced mesons are then to be detected by the GlueX detector system. Photons passing through the target without interaction will finally be collected in a photon beam dump located downstream (behind) the detector.

### 3.1.2 Calorimetry

Two electromagnetic calorimeter systems will be used in the GlueX detector: the BCAL and the FCAL. Neutral particles produced in the experiment will deposit their energy into one of these calorimeters allowing precise energy and timing (and therefore position) information to be gathered. The BCAL is also capable of detecting charged particles, but it is the neutral particle data that are particularly crucial, since they cannot be measured by other detector subsystems.

The LGD (Lead Glass Detector) used in the Brookhaven E852 experiment has been reconfigured to serve as the FCAL for GlueX and consists of 2800 individual lead-glass detectors, each  $4 \times 4 \times 45 \text{ cm}^3$ . These blocks are assembled in a circular array approximately 560 cm downstream of the target to cover polar angles of  $\theta < 11^\circ$ .

The BCAL is a sampling calorimeter composed of 48 trapezoidal modules, 390 cm long, arranged in a barrel formation. Each module is made by sandwiching layers of scintillating fibres (1 mm in diameter) between thin lead sheets (0.5 mm thick). The BCAL will be located immediately inside the 2.2 T solenoid, covering polar angles of  $11^\circ < \theta < 126^\circ$ . Because the BCAL is placed inside a 2.2 T magnetic field, constraints are placed on its readout. As the readout for the BCAL is the main subject of this thesis, it will be discussed in more detail later in this chapter.

### 3.1.3 Charged Particle Tracking

Located inside the BCAL, the CDC and FDC will be used to measure the energy deposition ( $dE/dx$ ) and spatial coordinates of charged particles passing through.

The CDC is a straw tube chamber consisting of over 3000 tubes arranged in a barrel with an inner radius of about 10 cm and an outer radius of about 55 cm. As charged particles are deflected by the magnetic field provided by the solenoid, they pass through the drift chamber, ionizing the gas that is inside of the straw tubes. By applying an electric field, the charge from ionization can be collected, allowing the particle's energy deposition to be measured and its path reconstructed. The CDC surrounds the target, being located in the upstream portion of the BCAL, and tracks particles in polar angles of  $20^\circ < \theta < 170^\circ$ .

Operating by the same principles, the FDC is a set of four disk-shaped drift chambers with outer radii of 60 cm, which are located within the downstream portion of the BCAL. Charged particles traveling in the angular range of  $2^\circ < \theta < 20^\circ$  traverse the FDC en route to the TOF and FCAL and thus have their trajectories reconstructed.

### 3.1.4 Particle Identification

Time-of-flight information, used for particle identification (PID) will be gathered using the TOF wall, located in front of the FCAL and covering polar angles of  $\theta < 11^\circ$ , and a start counter made of plastic scintillator strips, immediately surrounding the target. Two walls of scintillation bars  $2.54 \times 6 \times 252 \text{ cm}^3$  (thickness  $\times$  width  $\times$  length) in size, oriented orthogonal to one another to make an x-y plane, form the TOF wall. Other information necessary for PID will be gathered from other components of the GlueX detector including  $dE/dx$  information from the CDC and BCAL, and timing information from the BCAL. While the GlueX detector has been designed to achieve the physics goals of GlueX, space has been left between the solenoid and the TOF

wall for future PID detector systems.

## 3.2 The GlueX BCAL

The focus of the University of Regina's group within GlueX is the BCAL, which has been designed based on the electromagnetic calorimeter used in the KLOE experiment [14]. As photons are only measured by the FCAL and the BCAL, photon measurements provided by the BCAL are particularly important. Schematic views of the BCAL can be seen in Figure 3.2.

The BCAL is a group of 48 modules arranged in a barrel-shaped formation. Each module comprises a matrix of lead and scintillating fibres, and is built by alternating layers of *swaged* lead (lead plastically deformed with grooves along its length to accommodate fibres) and 1 mm-diameter scintillating fibres. These layers are bonded together by an optical epoxy<sup>1</sup>. Photosensors coupled to each end of the BCAL will provide energy and time measurements of photons resulting from the decays of photoproduced mesons.

A beam test of a prototype BCAL module was conducted in September 2006 [15], in part to determine the energy, timing and position resolutions of the calorimeter. Based on the number of photoelectrons yielded from the photosensors coupled to the module (which is based on the amount of light collected in scintillating fibres in the module), the energy resolution was determined to be  $\sigma_E/E = 5.4\%/\sqrt{E} \oplus 2.3\%$ . The time difference resolution is determined based on the speed of light in the module, and the double-ended readout of the calorimeter. It was found to be  $\sigma_{\Delta T/2} = 70 \text{ ps}/\sqrt{E}$ . From this information, the position resolution can be extracted ( $\sigma_z = 1.1 \text{ cm}/\sqrt{E}$ ), and the four momenta of neutral particles can be easily reconstructed.

The light output at either end of the module was also measured during the 2006

---

<sup>1</sup>Bicron BC-600 Optical Cement, Saint-Gobain Industrial Ceramics

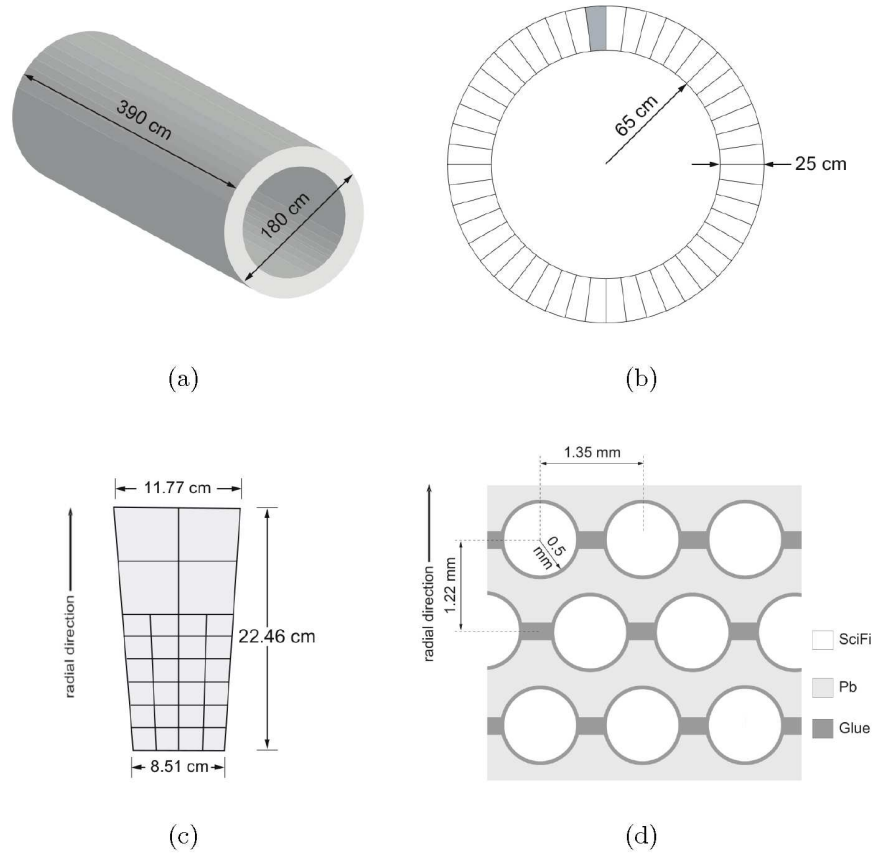


Figure 3.2: Views of the GlueX BCAL including (a) a schematic, (b) a BCAL module side view, (c) an end view showing all 48 modules and (d) an end view of one module showing the readout segmentation [11].

beam test using cosmic minimum ionizing particles (MIPs). The total number of photoelectrons per module end was determined. The experimental value agrees both with results obtained from Monte Carlo simulations, and with calculations based on fibre specifications like attenuation length and capture ratio [16, 17].

### 3.2.1 Scintillating Fibres

The scintillating fibres used in the BCAL are composed of three sections: a scintillating core and two layers of cladding (see Figure 3.3). The total fibre diameter is 1.0 mm with 0.03 mm and 0.01 mm thick first and second claddings, respectively [18]. The inner section, a polymer-based core, contains a combination of two fluorescent dopants (primary and secondary) selected to produce a specific wavelength of scintillation light. As an ionizing particle passes through the fibres, polymer molecules are excited. Energy is then transferred from the excited state of the polymer to the primary dopant via the Förster mechanism [19]. This is a non-radiative energy transfer. The primary dopant then emits a photon which is absorbed by the secondary dopant which, in turn, emits a photon with a longer wavelength than that of the original photon, which is either lost in the BCAL or propagated down the length of the fibre, depending on its angle of emission [20]. Photons will be totally internally reflected so long as they are emitted such that they reach the interface between the core and first layer of cladding at angles,  $\phi$ , less than the critical angle,  $\phi_C$ , where

$$\phi_C = \sin^{-1} \frac{n_2}{n_1} \quad (3.1)$$

and  $n_2$  and  $n_1$  are the indices of refraction of the fibre core and first cladding respectively. Each subsequent layer of cladding has a lower index of refraction than the previous layer, and thus serves to slightly increase the trapping efficiency of the



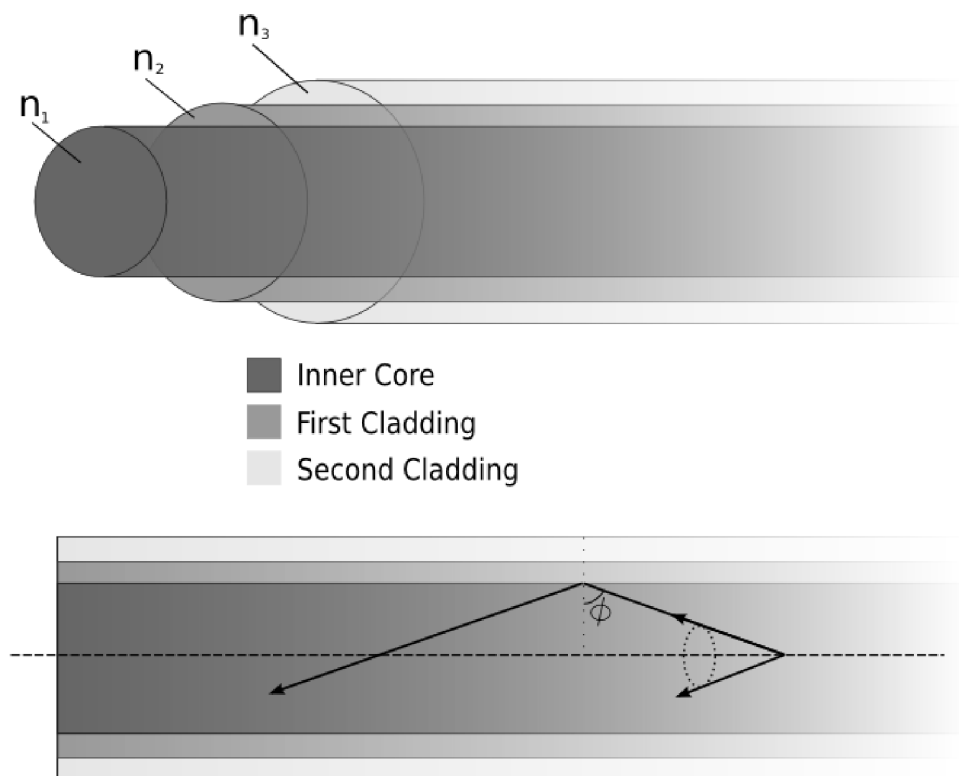


Figure 3.3: Diagram of a double-clad optical fibre (not to scale).

fibre. A typical trapping efficiency for a multi-clad fibre in air is between 5 and 10% per side. Because the optical epoxy used to bond lead and fibres together in the BCAL has an index of refraction higher than that of the outer cladding of a typical multi-clad fibre, some light will escape at the fibre-epoxy interface, slightly lowering the trapping efficiency of fibres in the BCAL.

### 3.2.2 Readout Requirements

The electronic readout for the GlueX BCAL has several requirements and challenges. The first difficulty arises based on the location of the BCAL within the larger detector. Because it is directly within the 2.2 T solenoid, the photosensors used must be resistant or, better still, immune to magnetic fields. Conventional photomultiplier tubes accelerate photoelectrons (produced when photons hit a photocathode) through a dynode chain resulting in amplifications as high as  $10^8$ . These devices require high voltages of around 2000 V, and are very sensitive to magnetic fields. While standard  $\mu$ -metal shields can be used to eliminate the effects of relatively small magnetic fields, they are no match for a 2.2 T solenoid.

Another challenge presented with the BCAL readout is space. Because the GlueX detector involves many individual components arranged in a relatively small area, the positioning of the readout for the BCAL must be carefully considered. Monte Carlo simulations have been carried out to determine the optimal BCAL readout segmentation [21]. Since it is crucial to capture the early part of electromagnetic showers in the BCAL (where most of the energy is deposited) to achieve the required energy and spatial resolutions, the innermost section (roughly half) of the BCAL should be outfitted with 24 photosensors per module, each approximately  $2 \times 2 \text{ cm}^2$  in area. The segmentation requirements for the outer region of the BCAL are less imposing since this area is only responsible for measuring any remaining energy deposited in

the BCAL. It has been shown that segmentation as coarse as four photosensors per module end would suffice (see Figure 3.2(c) on page 20). This means that each BCAL end must accommodate over 1300 photosensors. Either the photosensors used must be compact, fitting in a small area at the end of the BCAL, or light guides must be designed to carry scintillation light from the BCAL to photosensors located further away from the detector where more space is available.

Aside from the issues of location and magnetic fields, physics requirements are also placed on the readout for the BCAL. Since the fibres have a fairly small trapping efficiency, it is pivotally important to maximize the photon detection efficiency of the BCAL photosensors. The detectors also must be capable of detecting a broad energy range to maintain a reasonable energy resolution for the BCAL. The constant term in the energy resolution is largely affected by the detectors' minimum shower energy and dynamic range since these values dictate how much energy is lost in the detection process at the upper and lower ends of the total energy range. Ideally, the sensors' minimum energy threshold should be small enough to ensure that even low energy showers are detected, and the dynamic range of the detectors should extend past the maximum shower energy expected in the BCAL. GlueX is considering summing the inner readout cells in towers of three (see Figure 3.2(c) on page 20), resulting in a total of 12 segments per BCAL end instead of the originally proposed 28 segments, for purposes of broadening dynamic range and, of course, minimizing costs.

Detectors with fast timing characteristics ensure good BCAL time measurements. For GlueX, if traditional analog-to-digital converters (ADCs) are used, a rise time (the time taken for a signal to rise from 10% to 90% of its maximum amplitude) of less than 5 ns is ideal with a fall time (90% to 10%) of less than 30 ns. Currently another option, the use of Flash ADCs, is being considered, in which case longer rise times are desirable.

### 3.3 BCAL Readout Options

Two types of photosensors have been considered for use on the GlueX BCAL: Fine Mesh Photomultiplier Tubes<sup>2</sup> (FM PMTs) and large area Silicon Photomultiplier (SiPM) arrays<sup>3</sup>. While these options are both believed to be capable of satisfying GlueX's requirements for the BCAL readout, each one carries with it a set of challenges that the collaboration must deal with.

The FM PMT readout option delivers the familiarity and confidence of traditional photomultiplier tubes which are well-understood after years of use in countless experiments, but with the added feature that they are designed for use in environments with relatively high magnetic fields; however, FM PMTs are not immune to very large magnetic fields. They have been found to perform well in magnetic fields up to the order of 0.5 T as long as they are oriented at angles less than 40° with respect to the magnetic field [22]. For GlueX, this effectively means that light guides must be used to direct scintillation light away from the BCAL to a region just outside of the 2.2 T solenoid where residual fields are small enough for the FM PMTs to function well. Even outside of the solenoid, some attention must be paid to the orientation of the FM PMTs within the fringe fields [23]. The cost of these devices (several thousand dollars per detector), coupled with the added time and expense of developing a suitable light guide system (along with the inevitable efficiency losses inherent with any complex light transmission system), make FM PMTs an unfavourable solution for the BCAL readout, but a workable option nonetheless.

The immunity of SiPMs to magnetic fields is perhaps their most captivating feature, but they have other benefits that are of interest to GlueX. SiPMs are more compact than traditional PMTs, meaning that they not only have the fortitude to

---

<sup>2</sup>Hamamatsu R5924-70

<sup>3</sup>Hamamatsu MPPC, and SensL SPMPPlus

function within a 2.2 T field, but they can also physically fit in the space available at the ends of the BCAL. This means that light can be efficiently transmitted directly from the BCAL to the SiPMs using short light guides. SiPMs run at low voltages (between 20 and 70 V) and therefore do not require the high voltage supplies and cables needed for FM PMTs.

The hesitation to use SiPMs for the BCAL readout relates largely to the immaturity of the technology. Until recently, SiPMs have only been available commercially in sizes up to  $3 \times 3 \text{ mm}^2$ . This area is too small to be feasible for application on the BCAL, but in the past few years, the technology of large area SiPMs has developed substantially through the efforts of photonics companies like Hamamatsu and SensL. In particular, SensL has been working with GlueX to develop a SiPM array of 16 -  $3 \times 3 \text{ mm}^2$  devices arranged in a  $4 \times 4$  array. Several SensL SiPM devices and arrays have been tested in Regina. As new developments have been made in the production of SiPMs at SensL, these measurements have contributed to a determination of their suitability to the BCAL readout in terms of physics requirements, and are the focus of this thesis.

## Chapter 4

# Silicon Photomultipliers



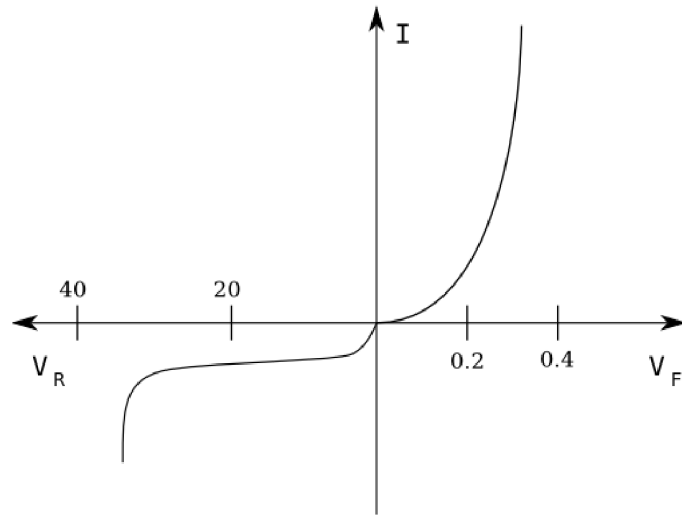
ingle-photon avalanche photodiode (APD) technology has been around since the 1960s, but the application of APDs in the field of scintillating light detection was first proposed in the Soviet Union in 1989 [24]. Since that time, great technological strides have been made, leading to the development of SiPM devices, composed of thousands of APDs, with areas of up to  $1 \times 1 \text{ mm}^2$ . These devices have been available commercially for some time, and devices with area  $3 \times 3 \text{ mm}^2$  have been developed, but in recent years demand for even larger area SiPMs has been ever intensifying. The large area SiPMs that the GlueX collaboration is considering today are arrays of  $3 \times 3 \text{ mm}^2$  SiPM cells, with a total area of  $1.2 \times 1.2 \text{ cm}^2$ . Many of the devices and arrays tested at the University of Regina are prototypes sent from SensL, as part of their collaborative research and development process with GlueX. To explore the operation of these large area SiPM arrays, it is appropriate to begin with the most elemental component - the APD.

## 4.1 Avalanche Photodiodes

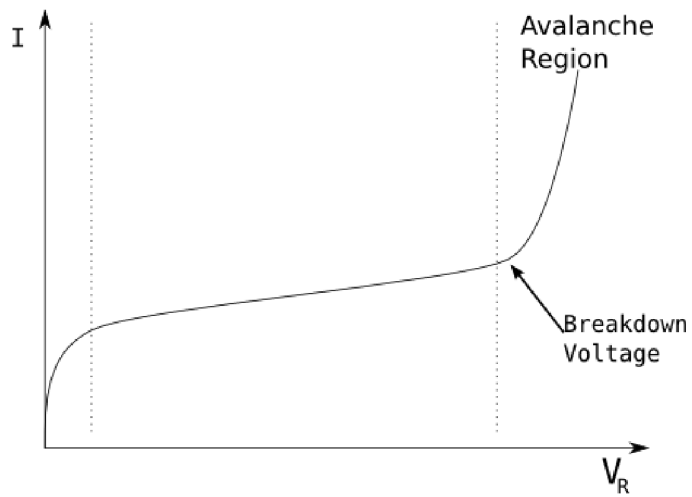
The APD is a solid state device similar to any other  $p - n$  junction. Diodes are typically operated in a forward bias mode, where current flows from the  $p$  (hole-rich, electron-deficient) to the  $n$  (electron-rich) side of the junction. Electrons flow much more easily in the  $n$  to  $p$  direction than the  $p$  to  $n$  direction, so diodes are often considered one-directional. Operated in reverse bias mode, only a small leakage current flows through the semiconductor until the reverse bias is large enough to cause the diode to break down (see Figure 4.1(a)). This breakdown voltage decreases with increased temperature. It is beyond the breakdown point, in the avalanche region (see Figure 4.1(b)), that APDs find their function.

At a reverse bias greater than the breakdown voltage, electron-hole pairs (carriers) can be excited by photons incident on an APD. APDs are thin, so even a relatively small potential (less than 50 V) over a short distance (on the order of  $\mu m$ ) results in an electric field of the order of  $10^6$  V/m. The electron from an excited electron-hole pair is accelerated by this large electric field, gaining kinetic energy as it travels. It can gain sufficient energy to excite additional electron-hole pairs in the  $p - n$  junction, and so on. This *avalanche* of electrons is referred to as a Geiger-type discharge. The probability of creating such an avalanche increases with increased *overbias* (voltage above the breakdown voltage), which results in increased *gain* (the amount of charge generated from an avalanche initiated by a single photo-generated carrier).

Once an avalanche is initiated, it can only be stopped, or *quenched*, if the bias drops below the breakdown voltage either by an external resistor or by quenching electronics. APDs operated in this *limited* Geiger mode typically amplify the charge of a single photoelectron by a factor of  $10^6$ . Quenching the avalanche ensures that the number of accelerated electrons, and therefore the current, generated from an avalanche in a particular APD will be nearly the same each time, regardless of the



(a)



(b)

Figure 4.1: Typical IV characteristic of an APD. The curve in (a) shows the behaviour of an APD in forward bias (first quadrant) and reverse bias (third quadrant), while (b) shows only the reverse bias IV characteristic (hereinafter, reverse bias and current shall be taken as positive values), illustrating the region of avalanche breakdown.



number of photo-generated carriers that initiate the avalanche. This gain is directly related to the APD's operational overbias by the equation

$$G = \frac{C \cdot (V - V_{br})}{q} \quad (4.1)$$

where  $G$  is the gain,  $C$  is the APD capacitance,  $(V - V_{br})$  is the overbias, and  $q$  is the charge of an electron. Because the gain is the same for any avalanche that is initiated, each APD acts as an independent photon Geiger counter. While the current induced in APDs is not proportional to the incoming photon flux (it is the same whether one or many photons initiate the avalanche), these detectors can efficiently detect single photons. When an avalanche is initiated in the APD, a photon is counted.

There are obvious limitations inherent to individual APDs. They are extremely small (mere micro-metres in diameter) and are only capable of detecting one photon at a time; however, for many applications these issues can be overcome by composing a larger SiPM device of hundreds or thousands of APDs.

## 4.2 Silicon Photomultipliers

SiPMs are essentially analog devices composed of binary elements (APDs or *pixels*). Each pixel remains in its “off” state (low current; high electric field) until a photo-generated carrier initiates a Geiger avalanche sending the pixel into a high current, “on” state. The output current from each pixel in a SiPM is sent to a common point, thereby summing all of these digital signals together and forming an analog signal that can be measured to determine the total energy (and therefore the number of photons) detected by the SiPM.

A schematic representation of a single pixel as part of a SiPM can be seen in Figure 4.2. Pixels, each composed of a  $p - n$  junction, are deposited on a silicon

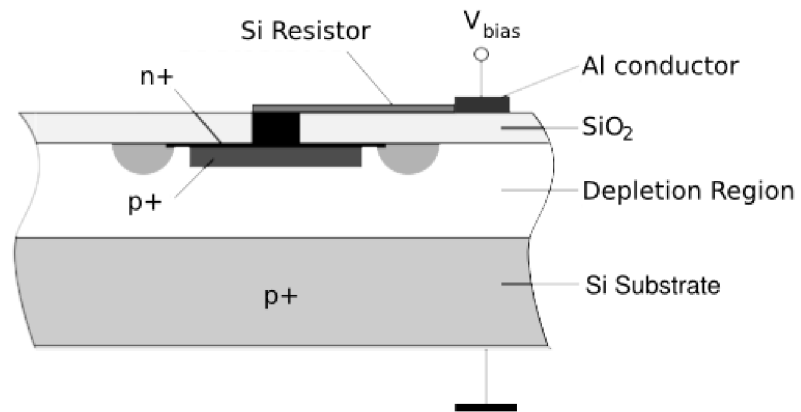


Figure 4.2: SiPM topology schematic showing a single pixel (APD) as part of a larger device.

substrate which has been treated with a  $p$ -type dopant. The breakdown voltage of a device is determined by the dopant concentration in the substrate. The region between the substrate and the pixel itself is the *depletion region*. After an excited electron-hole pair reaches the depletion region, the large electric field accelerates the electron through the device. If the electron gains enough energy to excite additional electron-hole pairs, a self-sustaining avalanche may begin. This avalanche is quenched by a silicon resistor connected in series with the pixel, thus forcing the high avalanche current through the quenching resistor and effectively lowering the bias voltage below the breakdown level, making this a limited Geiger-mode avalanche. An aluminum conductor coupled to each pixel carries the resulting current from avalanches in any pixel on the SiPM. From the summed signal, the total number of pixels fired in the SiPM, and therefore the number of photons detected, can be determined [25–28].

These multi-pixel devices are much more useful than APDs because of their increased active area and ability to detect more than one photon at a time, but there are several issues worth noting with their construction.

### 4.2.1 Cross Talk

One concern when grouping many pixels in a relatively small area is cross talk. Electrons traveling quickly through material (not unlike those electrons accelerated by the electric field in an APD) occasionally produce new photons through interactions with that material. Because the pixels in a SiPM are next to one another, those photons produced by an avalanche in one pixel can diffuse into neighbouring pixels, triggering additional avalanches and resulting in multiple pixels firing from a single photon.

Typically, less than 5% of photons result in cross talk, but this can be reduced by optical barriers between adjacent pixels. One solution is to cut trenches in the substrate between pixels, making photons less likely to travel from one pixel to the next.

### 4.2.2 Dark Rate

Another factor which must be considered is dark rate, the main source of noise in SiPMs. The dark rate is the number of false photons counted per second. Even in the absence of light, avalanches can be triggered in pixels by thermally generated electrons in the  $p - n$  junction depletion region, resulting in a false “photon” being counted. This can happen through thermal processes like Auger recombination, the spontaneous emission of electrons from atoms [29], or the Shockley-Read-Hall process, the excitation of electrons caused by defects or impurities in the silicon lattice [30].

Because these processes are triggered by defects and high temperatures, the dark rate is dependent on the purity of the silicon as well as temperature. The silicon purity is determined during production, but many SiPM electronics have cooling options to counteract the effects of a high dark rate, increasing the signal-to-noise ratio. With a temperature decrease of 20°C, the dark rate of a SiPM can be reduced by a factor of 10. While the electronics proposed for GlueX do not include cooling for each individual SiPM, a mass cooling option is being considered. By setting a discriminating threshold just above the dark noise level, the effects of dark events can be avoided, but this increases the minimum number of photons that can be detected by a device.

### 4.2.3 Photon Detection Efficiency

The photon detection efficiency (PDE) is defined as the ratio of the number of pixels fired in a SiPM device to the number of incident photons. The PDE depends on several factors and can be given by the equation

$$PDE(\lambda, V) = \eta(\lambda) \cdot F \cdot \epsilon(V) \quad (4.2)$$

where  $\eta$  is the quantum efficiency of the silicon for a particular wavelength  $\lambda$  region,  $F$  is the geometric fill factor, and  $\epsilon$  depends on the operational bias  $V$  and is the probability of a photon initiating a Geiger-mode discharge. These factors are expanded upon below.

The *quantum efficiency* of the silicon is defined as the percentage of incident photons which excite an electron-hole pair in a pixel. Photons with different energies will have different probabilities of exciting an electron-hole pair, and, as a photon's energy depends on its wavelength by the equation

$$E_\gamma = \frac{hc}{\lambda}, \quad (4.3)$$

this means that quantum efficiency is also a function of wavelength. This relationship can be mapped out to determine the spectral response of a device. A typical spectral response curve can be seen in Figure 4.3. The quantum efficiency of a SiPM can be as high as 70% in its peak spectral region, which implies that the factors limiting PDE are primarily the detector's avalanche probability and fill factor.

Once an electron-hole pair is excited,  $\epsilon(V)$  represents its likelihood of triggering a self-sustaining avalanche in the pixel. Just as the gain of a pixel increases linearly with overbias, so does its *avalanche probability*. Thus, an increase in overbias will cause an increased output for two reasons - increased gain causes higher charge amplification for each avalanche, and increased avalanche probability causes more photons to be detected. These positive effects of raising the overbias of a device are tempered by a corresponding increase in dark rate. For a specific application, an operational overbias can be determined where the balance of dark rate to gain and PDE is optimized.

The *geometric fill factor* is simply the ratio of the total active area of a SiPM (based on the active area of each pixel in that SiPM) to its total area. This depends on the size of the APDs used and their spacing in the device.

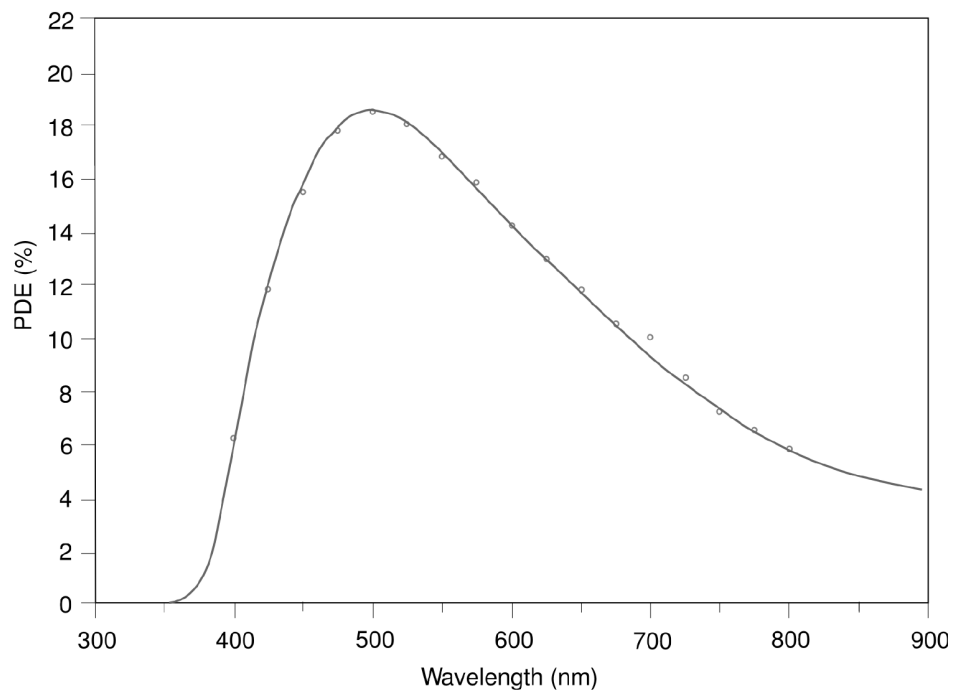


Figure 4.3: Typical spectral response of a SiPM device. Here the quantum efficiency, avalanche probability and geometric fill factor have all been folded into a measure of PDE [31].

Higher PDE values are beneficial for any experiment since it is ideal to detect every photon incident on a detector, but at the very least, the PDE must be well understood. A PDE in the range of 10-25% is characteristic of many SiPMs.

#### 4.2.4 Recovery Time

Pixels in SiPMs are capable of efficiently detecting single photons by initiating a Geiger-type discharge, as hereinabove discussed. This detection process is not instantaneous, and each pixel requires a certain amount of time to recover to a photon sensitive state, depending on how long it takes to recharge the pixel's capacitance. This recovery time limits the bandwidth of the detector as a whole.

A typical value of a pixel's recovery time is roughly 50 ns [31]. Assuming that each pixel in a SiPM is triggered at the same time, with a recovery time of 50 ns per pixel, a count rate of 20 MHz can be achieved. This is the limiting saturation condition, and represents the minimum count rate for a multi-pixel SiPM. As most signals will not trigger every pixel, pixels in the low current "off" state are ready to be sent into the high current "on" state, even while fired pixels are recovering from the previous event. Thus, the effective count rate of a SiPM can be higher than the minimum rate of 20 MHz determined by the saturation conditions.

#### 4.2.5 Linearity

Linearity of a SiPM device implies that every time a pixel is fired, that pixel's avalanche has been triggered by one and only one incoming photon. For low numbers of incident photons on a SiPM device, a linear response is usually achieved, and the current output of the SiPM is proportional to the incoming photon flux. This current  $I$  can be given by

$$I = \frac{N_\gamma}{s} \cdot PDE \cdot G \cdot q \quad (4.4)$$

where  $\frac{N_\gamma}{s}$  is the number of incident photons per second,  $PDE$  is the photon detection efficiency,  $G$  is the gain of each pixel, and  $q$  is the charge of an electron.

As long as a SiPM device's output current has a linear response and is proportional to the incident photon flux, a determination of the number of photons that were in the optical signal is trivial; this is not the case, however, if a detector is operated outside its region of linearity.

A SiPM's response will be linear provided only one photon is incident on any one pixel in the device per pixel recovery time. If more than one photon is incident on a single pixel, or if additional photons are incident on that same pixel before it has had time to return to its photosensitive state, then only one photon will be counted, even though several photons may have contributed to that single pixel avalanche. As the photon flux increases, it becomes more likely that multiple photons will contribute to a single pixel avalanche, resulting in a current output that is disproportional to the number of incident photons (see Figure 4.4). Another factor which affects the linearity of a SiPM device is cross talk, where one photon can result in multiple pixels being fired, but this is a more random effect.

The upper limit of the linearity region of a SiPM is determined by the saturation condition where one photon is incident on each pixel with a frequency of the inverse of the pixels' recovery time, by an optical signal uniformly distributed across all pixels in the device. It is imperative to operate a SiPM device within its region of linearity in order to obtain reliable information from its current output. The specifications for the GlueX BCAL readout require better than 10% linearity.

#### 4.2.6 Dynamic Range

The dynamic range of a SiPM depends on both the number of pixels in the device and its photon detection efficiency,  $PDE$ . Since only one photon can be counted by



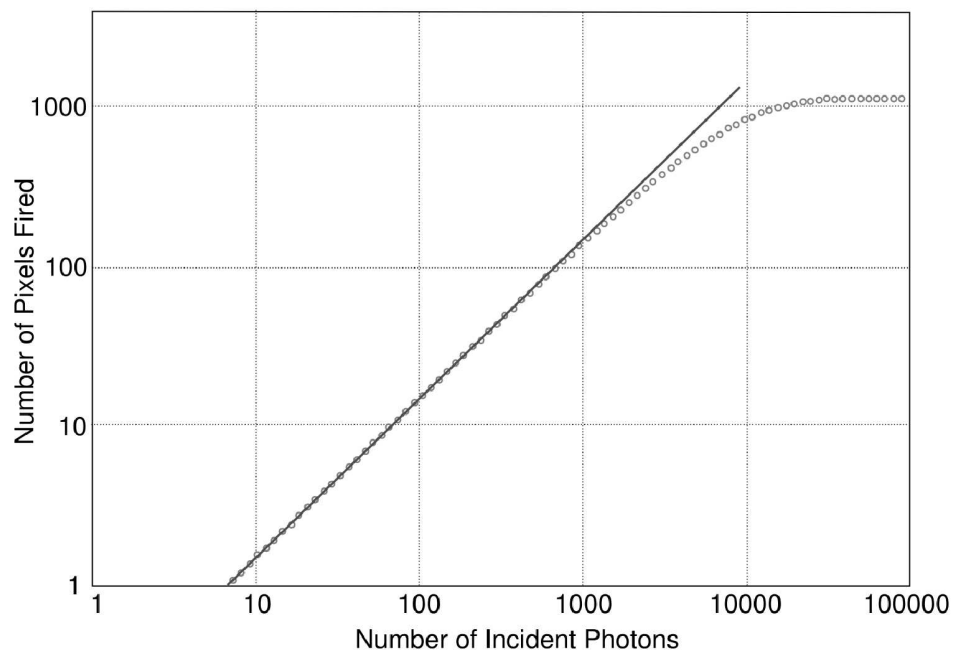


Figure 4.4: Response showing linearity of a typical SiPM device comprising, in this case, about 1100 pixels. Note that deviations in linearity become significant as the number of incident photons approaches the number of pixels in the device [31].

an individual pixel at a time, and since the number of photons detected is given by the product of the number of incident photons,  $N_\gamma$ , and the PDE, then the ratio of this product to the number of pixels,  $m$ , must be less than one:

$$\frac{N_\gamma \cdot PDE}{m} < 1. \quad (4.5)$$

A requirement on the dynamic range is that it is greater than the maximum number of photons expected to reach any given SiPM. For the GlueX BCAL, this number has been estimated at around 10,000 based on the number of photons expected to reach the central SiPMs of any given array. The arrays proposed for the BCAL each have over 50,000 pixels. Optimistically assuming a PDE of 20%, this results in a dynamic range of  $N_\gamma < 250,000$  photons. Clearly, the GlueX experiment is not expected to test the reaches of SiPM dynamic range.

### 4.3 SiPM Arrays

For the GlueX BCAL, the readout segmentation area is roughly  $2 \times 2 \text{ cm}^2$  for each SiPM. This area was selected to deliver acceptable detector tracking resolution, while requiring a reasonable number of photodetectors per BCAL module. Another factor in determining the readout segmentation was the cost of the photosensors and associated electronics. Until recently, the largest SiPM devices available commercially were  $3 \times 3 \text{ mm}^2$ , but, partly because of GlueX's requirements, the technology has evolved to the point where large area SiPM arrays of up to area  $1.2 \times 1.2 \text{ cm}^2$  are being manufactured. Each array is composed of 16 individual SiPM devices arranged in a  $4 \times 4$  matrix. These arrays can be read out either by 16 individual outputs, each corresponding to one SiPM element, or by one summed output.

The reduction in area from the  $2 \times 2 \text{ cm}^2$  segment on the BCAL to the  $1.2 \times 1.2 \text{ cm}^2$

active area of a SiPM array is accomplished by the combination of an acrylic light guide terminating into a Winston cone [32] collector with an overall transmission efficiency of about 95%.

Naturally, SiPM arrays have the same issues as individual SiPM devices, but on an elevated scale. The dark rate of an array with 16 devices is, understandably, about 16 times larger than that of an individual SiPM device. Also, the total effective capacitance of a SiPM array, again being much larger than that of an individual SiPM device, results in a slow recovery time for SiPM arrays. These are expected complications, but an additional challenge when combining many SiPM devices into larger arrays is ensuring a uniform response in all parts of the detector. Ideally, each element of the array would have a low dark rate so that the summed dark rate is not unreasonable. Also, each element should have the same breakdown response and photon detection efficiency, as it is pivotal that each SiPM device within an array produces the same signal amplitude for a given light intensity. This requires a high degree of precision in the production and doping of silicon wafers so that each part of the detector has a similar dopant level and concentration of defects or impurities.

### 4.3.1 Gain Uniformity

The *gain uniformity* of a SiPM array is a measure of the difference in signal amplitudes in different elements of the same array. Seeing as the gain is affected significantly by breakdown voltage (a device operated at 3 V above breakdown will have higher gain than one operated at 2 V above breakdown), and because each array is operated at a bias voltage common to all 16 elements, any difference in the breakdown voltage from one element to another can have a large affect on the gain uniformity of the array as a whole. This problem can be further aggravated as the overbias of a device also affects the PDE of that device. For GlueX, the desired gain uniformity is  $< 10\%$ .

## 4.4 Measurements of Performance

To evaluate the performance of a SiPM device or array, certain parameters must be measured. As a first step, the basic functionality of a device can be established by measuring its output current at different bias voltages in the absence of light, producing an IV (current versus voltage) curve. This determines the SiPM's breakdown voltage and provides a measure of the dark current of a device. Any major issues in the operation of a SiPM would most likely be manifested in an IV curve, either by the absence of a breakdown point, multiple breakdown points, or an unreasonably high dark current level. Between an IV curve and qualitative analysis of SiPM signals on an oscilloscope, the SiPM device's general performance level can be established.

Other SiPM performance parameters, which are pertinent for the GlueX collaboration specifically, are the PDE and the gain uniformity of SiPM arrays. While manufacturers usually provide an estimate of the PDE of their SiPM devices, it is prudent to complete measurements under conditions that closely simulate actual experimental conditions. For GlueX, this means determining the PDE of SiPM devices with scintillation light, as it will exit the BCAL. This can be accomplished through the use of scintillating fibres similar to those used in constructing the BCAL.

For SiPM arrays, the primary consideration is gain uniformity. This can be tested by applying a uniform light source to each individual element of an array, and even to different areas of a single element, and observing the output signals on an oscilloscope. Because the signal amplitude is affected by many characteristics contributing to a SiPM's performance including gain, overbias and PDE, gain uniformity implies consistency in each of these parameters.

Regina's contribution to the research and development of SiPM arrays largely relates to the independent measurements of these types of parameters. A description of the experimental procedures and results of those measurements is presented forthwith.

# Chapter 5

## SensL SiPMs in Regina

### 5.1 Introduction



iPMs are being considered for use on the BCAL for the GlueX experiment because of their immunity to magnetic fields, low bias voltage (around 30 V) and compact packaging. Tests have been ongoing at the University of Regina in an effort to evaluate the suitability of SiPMs as the GlueX BCAL readout.

In an attempt to satisfy the GlueX design requirements for the BCAL readout, SensL, a photonics company located in Ireland, has been developing a large area SiPM detector over the past several years, and has provided the GlueX group at the University of Regina with a diverse spectrum of silicon photomultiplier samples ranging from individual  $1 \times 1 \text{ mm}^2$  and  $3 \times 3 \text{ mm}^2$  SiPM devices (hereafter referred to as SPMMicros in keeping with SensL's nomenclature) to full  $4 \times 4 - 3 \times 3 \text{ mm}^2$  SiPM arrays with built-in electronics systems. SPMMicros have been available commercially from SensL for many years, and through significant performance optimization efforts, partly in collaboration with GlueX, SensL SiPM arrays have also recently become available.

The characterization of these devices in Regina has provided valuable feedback to

the GlueX collaboration, as SiPM arrays are considered for the readout of the GlueX BCAL. These measurements have included IV characteristics, qualitative analysis of signals and individual photoelectron detection capability, PDE of SPMMicros, and gain uniformity of SiPM arrays.

Current versus voltage relationships are crucially important in the characterization of any SiPM. While manufacturers provide a suggested SiPM operating overbias along with each SiPM's breakdown voltage,  $V_{br}$ , an independent IV characteristic measurement can verify  $V_{br}$ . Because the breakdown voltage is highly temperature dependent, even a small difference in ambient conditions can affect it. Any change in  $V_{br}$  from manufacturers' specifications then affects the operational voltage of the SiPM as well. IV characteristics also provide a baseline measurement of the dark current in a SiPM. As dark rate (and therefore dark current) should scale linearly with active area, a comparison of IV curves from similar detectors with different active areas can verify that the dark rate in a particular detector is reasonable.

SiPM signals can be observed on an oscilloscope for qualitative evaluation. Here, rise and fall times can be measured, and, perhaps most importantly, the general signal shape can be observed. The timing requirements of SiPM signals are determined by the front end electronics, such as discriminators, analog-to-digital converters (ADCs), and time-to-digital converters (TDCs), but any abnormalities in the general shape of the signals are usually symptoms either of problems in the SiPM electronics, or of SiPM performance limitations in linearity or dynamic range.

In order for SiPM arrays to be used with the BCAL, their PDE must be well-understood. As long as the PDE is known, the number of incident photons can be easily determined from the current output of a SiPM. Manufacturers commonly quote PDE values for their devices, but as PDE depends on the wavelength of incoming photons (among other parameters) it is necessary to measure the PDE of SiPM devices

using a setup that closely resembles projected experimental conditions. In the case of GlueX, this means using real scintillation light emitted from optical scintillating fibres. Since SensL SiPM arrays are essentially compositions of SPMMicros arranged in a  $4 \times 4$  matrix (the silicon in a SPMMicro is treated the same way as in a SiPM array element), a measurement of SPMMicro PDE should also be valid for SiPM arrays.

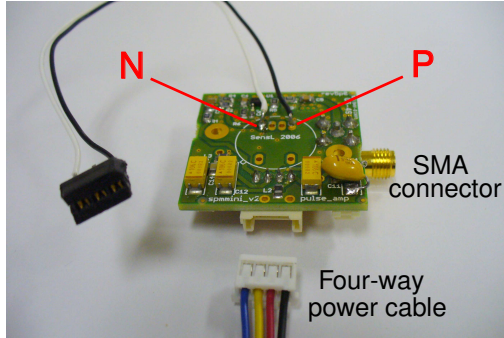
In SiPM arrays, not only must each element perform well, but the elements must also have comparable functionality. By applying a uniform light source (preferably scintillation light) to each element in an array and observing its signal amplitude on an oscilloscope, a measurement of gain uniformity can be made. Good gain uniformity is an indicator of other uniformities in the array elements including  $V_{br}$  and PDE. For GlueX, deviations in the gain from one element to another are required to be less than 10%, within each array.

In this chapter, the SiPMs tested at the University of Regina are introduced, and the experimental processes and results pertaining to measurements of current versus voltage characteristics, PDE, and gain uniformity are outlined.

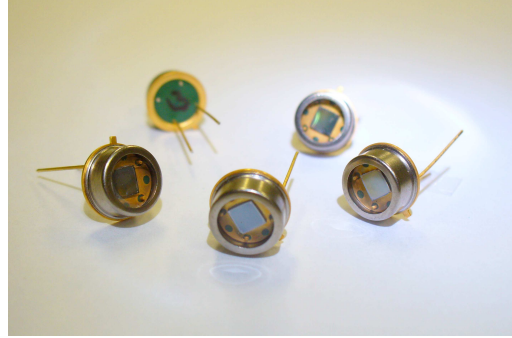
## 5.2 SPMMicros

Five types of SPMMicros were tested in Regina (see Figure 5.1). The nomenclature used by SensL to identify specific types of SPMMicros includes a prefix (1-mm or 3-mm) denoting the size of the device's total active area ( $1 \times 1 \text{ mm}^2$  and  $3 \times 3 \text{ mm}^2$ , respectively), a number (A35 or A20) denoting the size of an individual pixel ( $35 \text{ }\mu\text{m}$  and  $20 \text{ }\mu\text{m}$ , respectively), and a suffix (H or HD) denoting whether or not a device has gone through an additional silicon processing step called *gettering* (H devices have not undergone gettering).

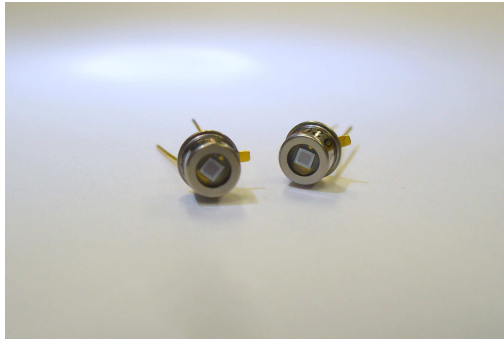
The IV characteristics of an initial shipment of 10 - 3-mm A35H devices were



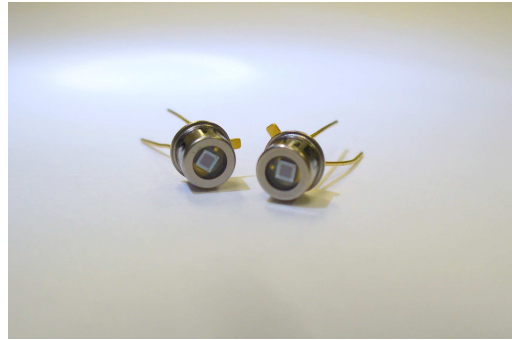
(a) SPMMicro electronic board



(b) 3-mm A35H



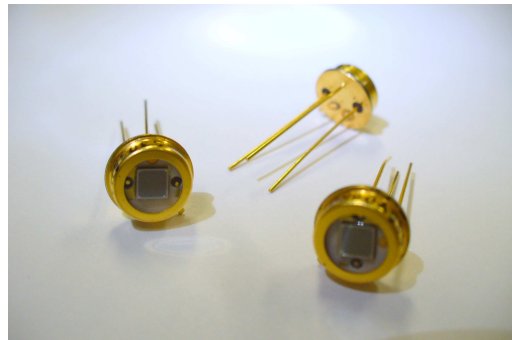
(c) 1-mm A20HD



(d) 1-mm A35HD



(e) 3-mm A20HD



(f) 3-mm A35HD

Figure 5.1: Photographs of SensL SPMMicros (and (a) electronic board) tested in Regina (original in colour).

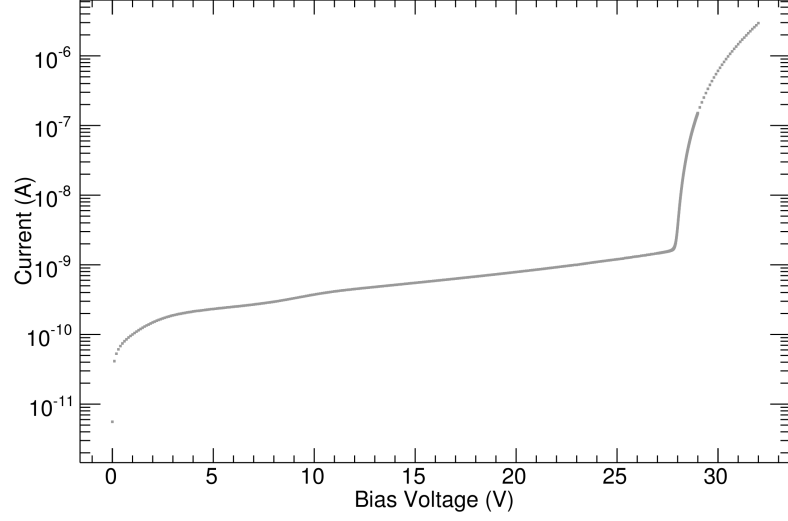


measured before the arrival of four other types of SPMMicros. The 1-mm A35HD, 1-mm A20HD, 3-mm A35HD, and 3-mm A20HD devices (the original A35H SPMMicros have a slightly larger fill factor than the A35HD devices) were tested to determine which type would be used as the basic element of SiPM arrays. All of these devices are sensitive to light in the spectral range of 400 - 1100 nm with peak spectral response at about 490 nm. Details regarding the detectors' fill factors, including pixel size, active area, and number of pixels per device can be seen in Table 5.1 on page 50.

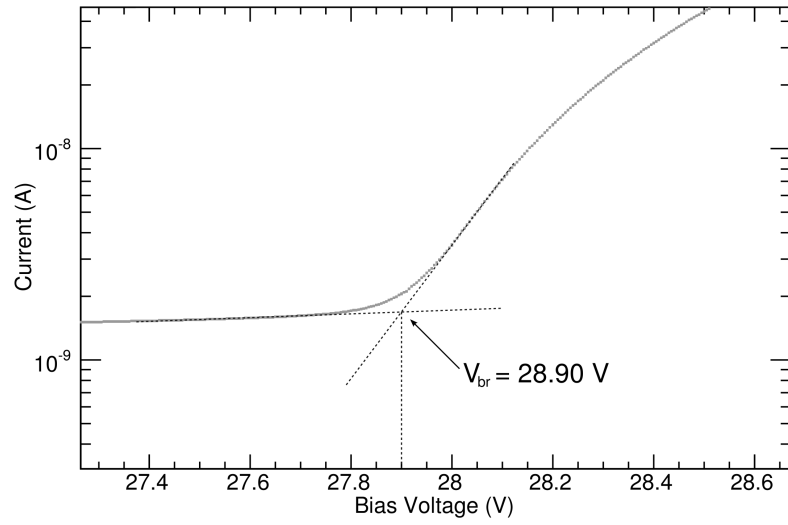
Each SPMMicro is equipped with two pins - an anode and a cathode (3-mm A20HD and A35HD devices also have a third ground pin). These can be connected to electronic boards supplied by SensL, which deliver bias voltage to, and amplify (by a factor of 20) the output of the SPMMicros. There are connection terminals on the electronic board for a four-way colour-coded power cable and an SMA signal output. The four-way power cable is used to supply power from external sources to the board. The red and yellow wires are powered at +5 and -5 V respectively and supply power to the amplifier within the board, while the blue and black wires are the bias (around 30 V) and ground connections, respectively (see Figure 5.1(a) for a photo of the actual board).

### 5.2.1 IV Characterization

Current versus voltage measurements are meant to quantify the leakage current present in a photodiode that is reverse biased, and to identify the point where the photodiode begins to break down. All of these measurements are taken in a dark environment. Measuring IV characteristics simply involves applying reverse bias voltages to a SiPM device directly using the anode and cathode pins on the SiPM housing. Connecting the SiPM in series with the voltage supply and picoammeter functions of a Keithley 6487 Picoammeter/Voltage Source (the Keithley can independently sup-



(a) Full IV Curve



(b) Breakdown Region

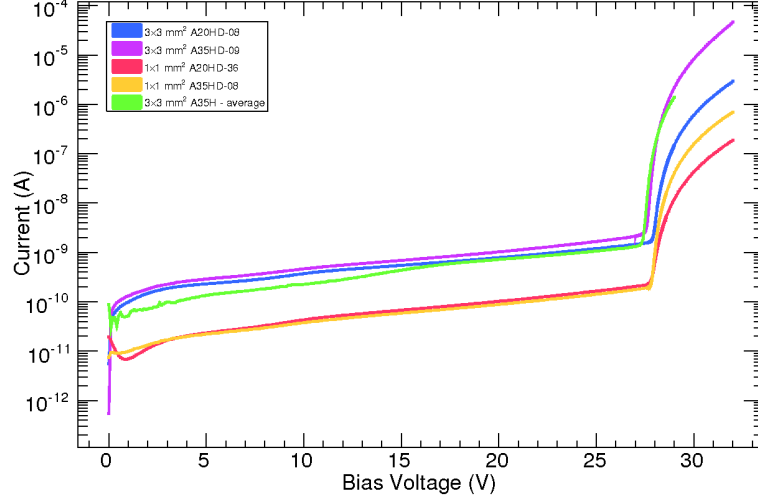
Figure 5.2: Typical IV curve of a 3-mm SPMMicro (in this case, 3-mm A20HD-08). The plots show measurements of (a) the full IV characteristic of the SiPM and (b) a close-up of the breakdown region illustrating the definition of the breakdown voltage.

ply voltage and measure current in a circuit) allows current versus voltage data to be collected. The Keithley can automatically increase the supply voltage by pre-set increments on regular intervals making the data acquisition process remarkably efficient.

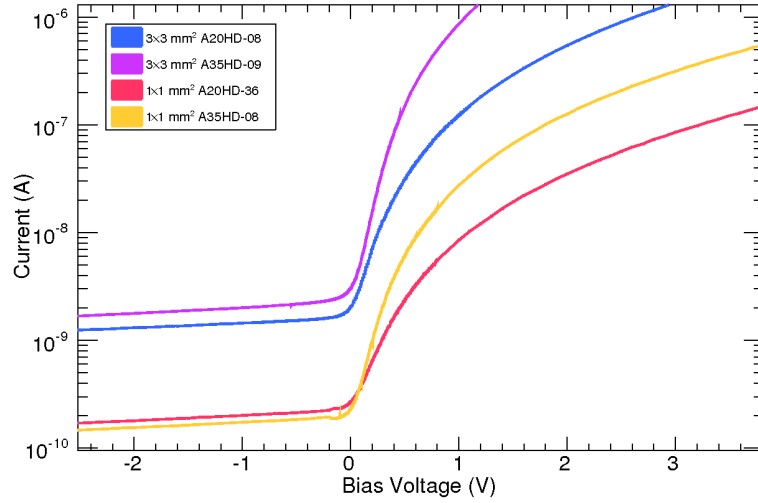
For these measurements, the supply voltage was typically increased at time intervals of 5 s allowing the Keithley time to accurately record the SiPM current. Since SensL SiPM breakdown voltages are usually around 28.0 V, voltage sweeps were done from 0 to 32 V (in most cases), with a typical IV curve shown in Figure 5.2(a). This allows the full IV characteristic to be observed, including the behaviour of the SiPM up to overbias voltages of about +4.0 V without risking the damage of a device by supplying large overbiases. After the breakdown voltage region from the initial voltage sweep was determined, more detailed measurements were conducted, with smaller voltage increments, focusing on that region.

Once the region of breakdown has been determined, two straight lines can be drawn from the data approaching the breakdown point from either direction. The point of intersection of these two lines defines the breakdown voltage (refer to Figure 5.2(b)). IV characteristics of all SPMMicros tested in Regina can be seen in Figure 5.3(a) with the resulting breakdown voltages listed in Table 5.1 on page 50.

Comparing the IV curves of these devices, ratios of the dark currents of A35HD to A20HD devices can be determined for both 1-mm and 3-mm geometries. This can be done by extracting the dark current from the graph for each device at the same overbias, after the IV curves have been normalized for breakdown voltages (see Figure 5.3(b)). As dark current is expected to scale with active area (the size of one pixel multiplied by the total number of pixels in a device), these ratios should be



(a) Representative IV curves of all SPMMicro devices



(b) Normalized IV curves of A20HD and A35HD devices

Figure 5.3: Sample IV characteristics of all SPMMicro types tested in Regina (original in colour), (a) including the average IV curve of all 10 3-mm A35H devices. Note that the dark current of 3-mm devices is larger by about an order of magnitude than the dark current of 1-mm devices. Plot (b) shows IV curves of A20HD and A35HD devices, normalized for their  $V_{br}$ .

Table 5.1: Characteristics of SensL SPMMicro devices including identification number, breakdown voltage ( $V_{br}$ ), active area, pixel size, number of pixels per device ( $m$ ), and fill factor. Note that the listed breakdown voltages are those measured in Regina.

SPMMicro	ID	$V_{br}$ (V)	Active Area	Pixel Size	$m$	Fill Factor
1-mm A35HD	08	27.80	$1 \times 1 \text{ mm}^2$	$35 \text{ }\mu\text{m}$	400	59%
	09	27.80				
1-mm A20HD	36	27.80		$20 \text{ }\mu\text{m}$	848	43%
	39	27.80				
3-mm A35HD	07	27.60	$2.85 \times 2.85 \text{ mm}^2$	$35 \text{ }\mu\text{m}$	3640	59%
	08	27.55				
	09	27.55				
3-mm A20HD	07	28.00		$20 \text{ }\mu\text{m}$	8640	43%
	08	27.90				

similar to the ratio of active areas:

$$\frac{A_{A35HD}}{A_{A20HD}} = \frac{35 \times 35 \mu m^2 \times 400}{20 \times 20 \mu m^2 \times 848} = 1.44. \quad (5.1)$$

The actual ratios for the 1-mm and 3-mm devices at a standard overbias of +3.0 V are 3.68 and 10.48 respectively. This indicates that the dark current increases significantly more than expected with active area, especially for the 3-mm devices tested in Regina. Clearly, this also indicates that the A35HD SPMMicros have sources of dark current beyond the “physics” sources outlined in Section 4.2.2. Any number of factors (including inefficient electronics, damaged pixels, or higher concentrations of impurities in the silicon) could contribute to this increase in dark current, but regardless of the source, it effectively decreases the signal-to-noise ratio, reducing the capabilities of A35HD detectors.

### 5.2.2 Qualitative Performance Evaluation

Once a SPMMicro’s functionality has been verified by an IV curve, its signal can be observed on an oscilloscope. The experimental setup for these observations begins by connecting the SPMMicro’s cathode and anode to the N and P contacts respectively on the electronic board (see Figure 5.1(a) on page 45). Power is supplied to the board through the four-way cable at some overbias using external voltage supplies<sup>1</sup>. By coupling an SMA-to-BNC adaptor to the SMA output of the electronic board, a 1.5 m long RG-58 coaxial cable can be used to transmit this output to an oscilloscope<sup>2</sup>. Signals from the SPMMicros are observed by coupling a scintillating fibre to a SPMMicro with a small amount of optical grease and applying laser light perpendicular to the fibre along its length.

---

<sup>1</sup>Regulated DC Power Supplies GP-1503 and CS13003X111 for the +5 and -5 V amplifier voltages, and the Keithley Power Supply for the bias voltage

<sup>2</sup>Tektronix TDS 5104 Digital Phosphor Oscilloscope

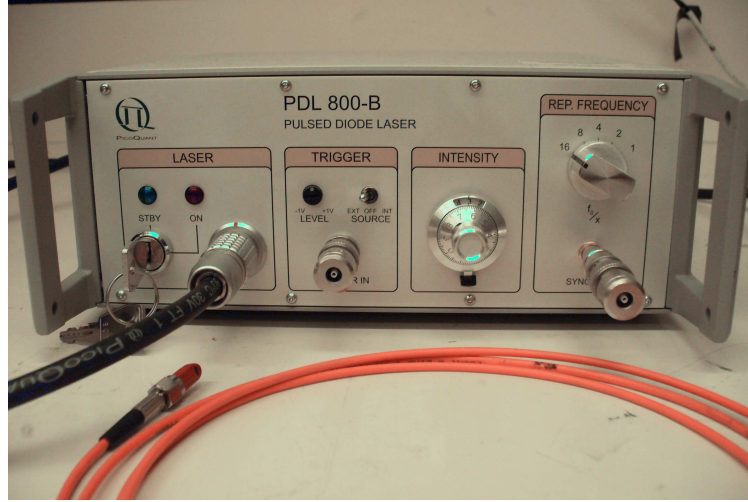


Figure 5.4: A photo of the PicoQuant laser used for SiPM tests in Regina (original in colour). The front panel of the laser driver can be used to adjust the laser light intensity (arbitrarily labeled from 0 to 10), the internal laser pulse frequency to frequencies of  $\frac{40 \text{ MHz}}{x}$  where  $x$  is 1, 2, 4, 8, or 16, or to externally trigger laser pulses using a gate generator. Also note the SYNC OUT output on the lower right-hand side of the panel. This output provides signals synchronized with the laser pulses.

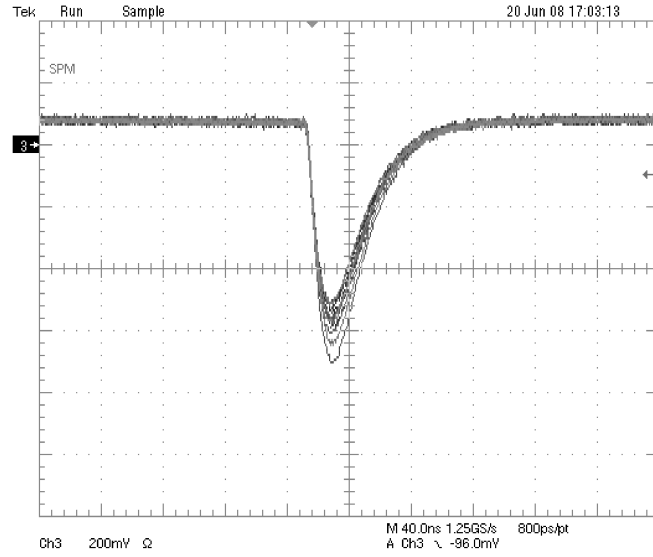
For many SiPM tests, ultra-violet laser light is used to illuminate an optical scintillating fibre coupled to the SiPM device of interest, thus applying light to the SPM-Micro active area. The laser used in Regina is a PicoQuant PDL 800-B Picosecond Pulsed Diode Laser with LDH-P-C-375B Laser Head (see Figure 5.4). It has a peak emission of photons with a wavelength of roughly 375 nm with a width of 60 ps, and has an adjustable intensity (arbitrarily labeled from 0 to 10) capable of emitting as low as one photon per laser pulse. The laser also has several pulse frequency settings ranging from 2.5 to 40 MHz, but external triggers can be used to induce other frequencies.

#### 5.2.2.1 Limits in Linearity

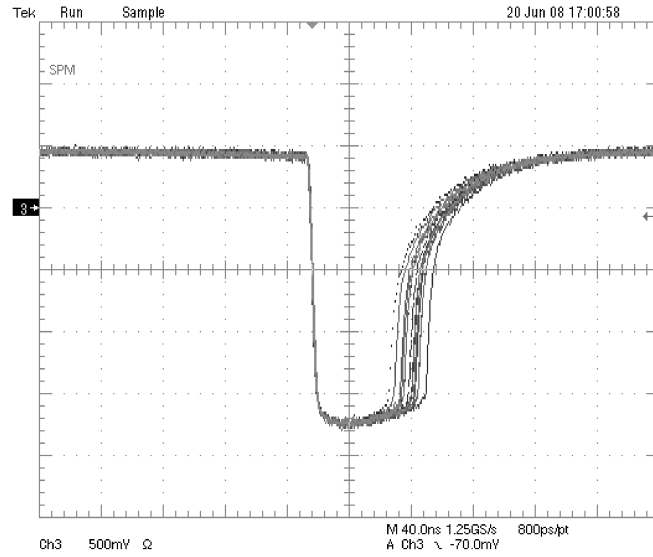
By adjusting the laser’s intensity, a range of operability can be established. A standard signal captured from the oscilloscope can be seen in Figure 5.5(a). For the 3-mm A20HD SPMMicro, at (arbitrary) laser intensities above or around 2.90, signal saturation is observed. This is manifested as a squared off signal (see Figure 5.5(b)). Saturation of the SPMMicro itself would be evidenced by a signal with constant amplitude (and shape) even with increased light intensity. This type of “chopped” signal is clearly indicative of saturation in the electronics rather than a limitation in the SPMMicro’s intrinsic dynamic range.

Limits in the linearity of SiPM devices hinge upon not only the incident light intensity, but also on the frequency of light pulses. For relatively high laser pulse frequencies, SiPM signals often exhibit a notable overshoot in the pulse tail, resulting in a baseline offset (see Figure 5.6(b) on page 55). The size, and therefore severity, of this offset increases with pulse amplitude, or light intensity, as expected. The effects of baseline offsets can be magnified if the effective recovery time of a SiPM device is increased by inefficient electronics. (The baseline offsets observed for SPMMicros in



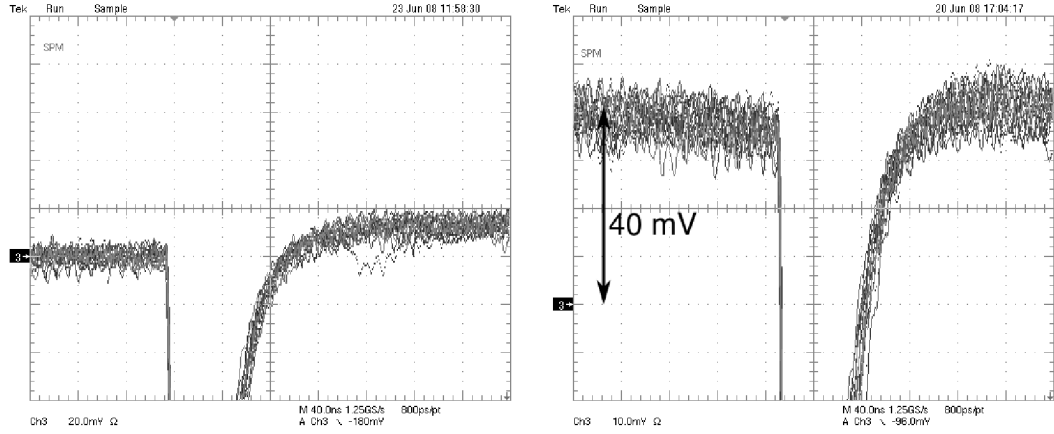


(a) Laser Intensity Setting 2.88



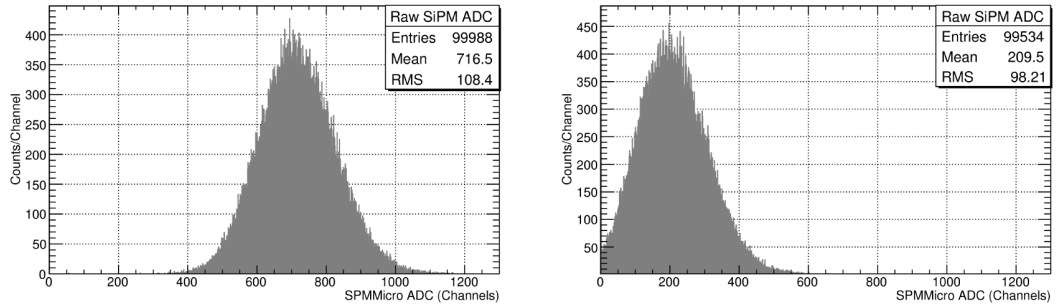
(b) Laser Intensity Setting 2.90

Figure 5.5: Sample scope traces from a SPMMicro device at laser intensity settings of (a) 2.88 and (b) 2.90 where the signal is saturated. For the 3-mm A20HD SPMMicro, this saturation occurs for laser pulses with  $\gtrsim 10,000$  photons per pulse. The major scale division in the horizontal axis is 40 ns, and on the vertical axis it is (a) 200 mV and (b) 500 mV.



(a) 1 kHz Signal

(b) 2.5 MHz Signal



(c) 1 kHz ADC Spectrum

(d) 2.5 MHz ADC Spectrum

Figure 5.6: Scope traces and ADC spectra at (left panels) low laser pulse frequency and (right panels) high laser pulse frequency. A baseline offset in SPMMicro signals at high frequency results in an ADC shift to the left on the ADC scale. Each of these measurements was taken at the same laser intensity and overbias. Note that there is a baseline offset of about 40 mV, resulting in a shift of the ADC mean of just over 500 channels. Note also that the width (RMS) of the spectrum remains largely unaffected by the shift.

Regina have been diagnosed as purely electronics-based, and are not based on any limitations in the functionality of the SPMMicros themselves.) At the low frequency of 1 kHz (achieved by triggering the laser externally using a gate generator) there is no shift even for high laser intensities (see Figure 5.6(a)), but at the relatively high rate of 2.5 MHz, offsets become significant at laser intensities greater than 2.60 for 3-mm A20HD devices.

As signals are read by an ADC unit, the current in that signal is integrated for a certain time called the *gate width*, measured in ns. The ADC scale is divided into channels, each representing a certain amount of charge. A signal, or entry, is assigned to an ADC channel based on the amount of charge measured in that signal. In this way an ADC histogram is formed (see Figure 5.6(c)). If a baseline offset is present in a signal, the total charge measured by the ADC is lessened by a fixed amount related to the signal offset, resulting in an ADC shift of the entire spectrum (see Figure 5.6(d)).

Based on the specifications of the particular ADC unit used, the expected ADC shift can be estimated from a measurement of the baseline offset of a signal. For the LeCroy 2249A ADC, the full-scale range is  $256 \text{ pC} \pm 5\%$  over 1024 channels, so the conversion factor is  $0.25 \text{ pC/Channel}$ . The impedance of the ADC is  $50 \Omega$ , so the pedestal position is shifted by a value  $ADC_{Shift}$  given by

$$ADC_{Shift} = \frac{Offset}{50 \Omega} \frac{Gate Width}{0.25 \text{ pC/Channel}} \quad (5.2)$$

where the Offset is found by viewing the baseline of the SPMMicro signal, and the Gate Width is set on the coincidence unit. For a gate width of 160 ns and a baseline offset estimated at 40 mV, this would result in an ADC shift of about 512 channels to the left, which corresponds with the shift seen in Figure 5.6(d).

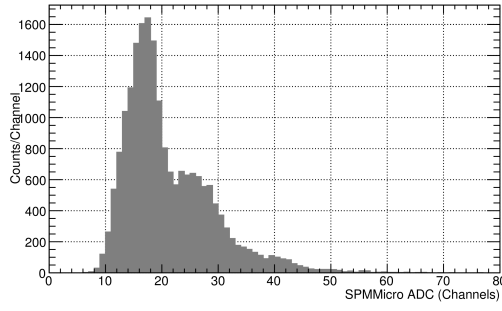
### 5.2.2.2 Individual Photoelectron Peaks

Operating a SPMMicro within its dynamic range and region of linearity, remarkable resolution results can be produced for low numbers of detected photoelectrons. Because any pixel fired produces roughly the same amount of current, the ADC spectrum from a SiPM signal is quantized into distinct peaks, with each subsequent peak representing an additional pixel fired by a photoelectron (or an additional photon detected). This quantized spectrum is overlaid on the non-zero dark current of the device, and since more pixels fired leads to more uncertainty in the output current of the SiPM device, the width of the peaks increases slightly with each additional peak. Thus, for large numbers of photoelectrons detected, the peaks merge into one another forming a more continuous spectrum, but for low numbers of photoelectrons, distinct peaks are observable.

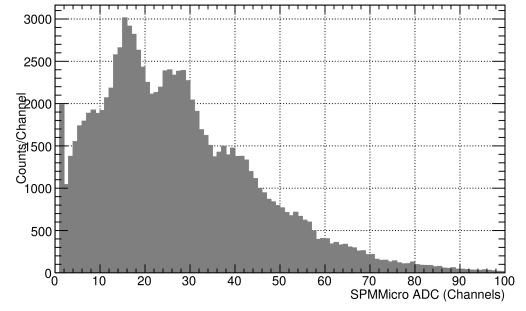
Sample ADC spectra for each A20HD and A35HD device can be seen in Figure 5.7. Individual photoelectron peaks can clearly be seen for all devices except the 3-mm A35HD SPMMicro. This can be attributed to the large increase in dark current over and above what the active area of 3-mm devices would justify. The decrease in the signal-to-noise ratio for 3-mm A35HD devices results in an inability to produce ADC spectra with distinct photoelectron peaks at room temperature.

### 5.2.2.3 Cooling Effects

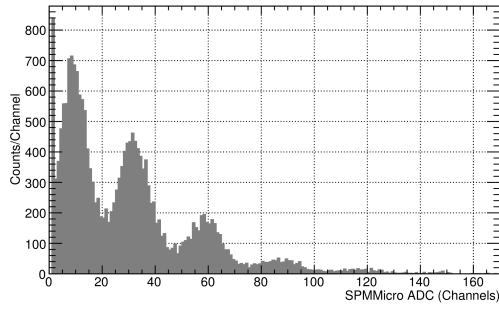
Since dark current is expected to decrease with decreased temperature, cooling tests were conducted. By adding dry ice to an insulated box housing the SPMMicro experimental setup (including the electronic board and scintillating fibre) with small holes cut to allow cables and the laser head to enter the box, the temperature of the SPMMicro was reduced from room temperature (about 25°C) to -20°C. ADC spectra were taken for the 3-mm A35HD device, with results shown in Figure 5.8 on page 59.



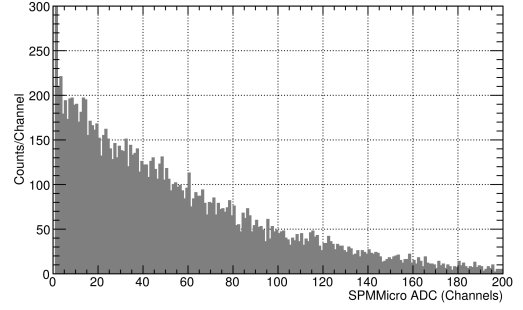
(a) 1-mm A20HD



(b) 3-mm A20HD

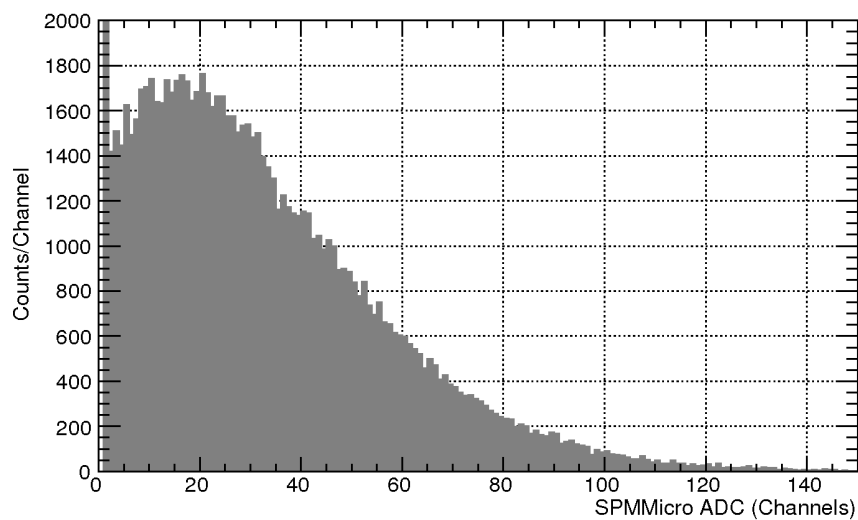


(c) 1-mm A35HD

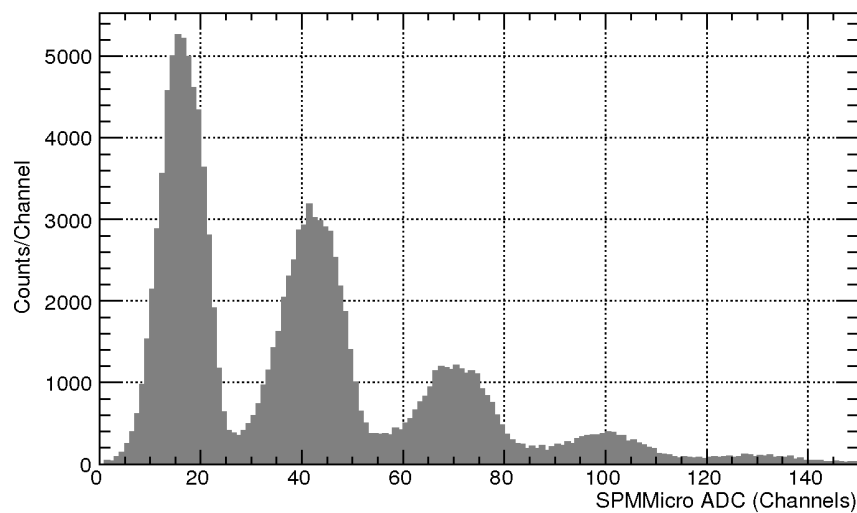


(d) 3-mm A35HD

Figure 5.7: Sample SPMMicro ADC spectra taken at room temperature, overbias +3.0 V, and laser intensity 2.40.



(a) Room Temperature



(b) -20°C

Figure 5.8: Cooling results for 3-mm A35HD SPMMicro devices taken at overbias +2.0 V, and laser intensity 2.40.

Furthermore, a sample screen shot captured over several seconds on the oscilloscope can be seen in Figure 5.9(a) where distinct bands are observable, each representing an additional photon detected by the SPMMicro. The corresponding ADC spectrum can be seen in Figure 5.9(b). These plots, taken at  $-20^{\circ}\text{C}$ , show that, in the absence of excess noise, A35HD devices are capable of excellent individual photoelectron peak resolution, but that small signal-to-noise ratios at room temperature diminish A35HD SPMMicro capabilities.

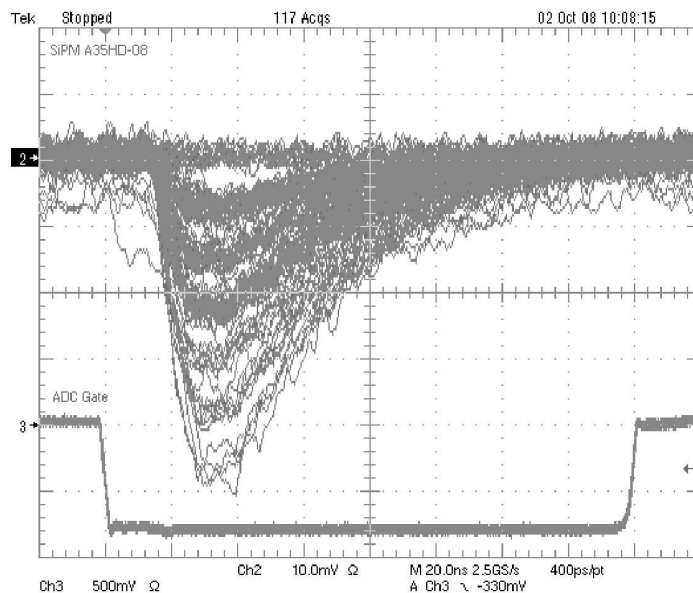
### 5.2.3 Photon Detection Efficiency

The PDE of any device is simply the ratio of the number of photons incident on a detector to the number of photons detected. For the GlueX experiment, since SiPM devices are proposed for the detection of neutral particles from optical scintillating fibres in the BCAL, it is ideal to use real scintillation light from fibres similar to those used in BCAL production to determine the PDE of a SiPM.

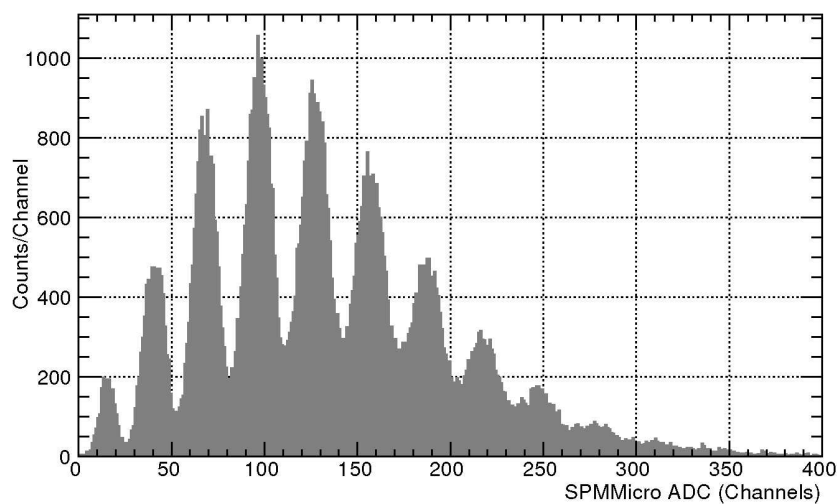
#### 5.2.3.1 Description of Experimental Setup

The calculation of the number of photons detected is relatively trivial, and the determination of the number of photons incident on a SPMMicro can be accomplished using a setup involving a calibrated photodiode. A scintillating fibre can be coupled at one end to a SPMMicro and, at the other end, to a calibrated photodiode. Applying laser light perpendicular to the centre of the scintillating fibre along its length allows the number of incident photons to be determined from the output current of the photodiode. This assumes that the scintillation light propagates identically down the length of the fibre in each direction.

For these tests, the PicoQuant laser was used to illuminate a short (30 cm) green



(a) SPMMicro Signal



(b) ADC Spectrum

Figure 5.9: Typical signal and corresponding ADC spectrum showing individual photoelectron peaks detected by a 3-mm A35HD SPMMicro at  $-20^{\circ}\text{C}$  with laser intensity 2.60.



scintillating fibre<sup>3</sup> at its centre. One end of the fibre was coupled to the calibrated photodiode<sup>4</sup>, which was connected to the Keithley picoammeter which read its current. The other end of the fibre was coupled to a SPMMicro device, which was connected to an electronic amplifier board (see Figure 5.1(a) on page 45). In each case the fibre was polished using a FiberFin polisher<sup>5</sup> and coupled to the SiPM and the photodiode using a small amount of optical grease.

Bias voltage was applied to the SPMMicro by the Keithley voltage source, and voltages of +5 and -5 V were applied to power the amplifier. The laser SYNC OUT (an output which provides signals synchronized with laser pulses) was used to start the ADC<sup>6</sup> gate after being passed through a discriminator<sup>7</sup> and a coincidence unit<sup>8</sup> to establish the gate width (all measurements were taken with ADC gate widths of either 120 ns or 160 ns). To lower the event rate in order to avoid saturating the ADC with events, a pulse generator<sup>9</sup> triggered by the laser SYNC OUT was used to produce a 1 ms pulse, which was then used as a veto in the coincidence unit. The SPMMicro signal was delayed by about 20 ns before being sent to the ADC unit. A photograph and a schematic diagram of the electronic setup for these measurements can be seen in Figure 5.10.

Working in a range of laser intensities from 2.20 to 2.88 that simultaneously generate current which can be read by the photodiode (very small currents  $\leq 20$  pA cannot be read reliably by the Keithley) **and** produce SPMMicro signals that are not saturated, as in Figure 5.5(b) on page 54, several measurements were taken to determine the PDE of a given detector.

---

<sup>3</sup>Saint-Gobain BCF-20 Fast Green Scintillator

<sup>4</sup>Hamamatsu S2281 Calibrated Photodiode

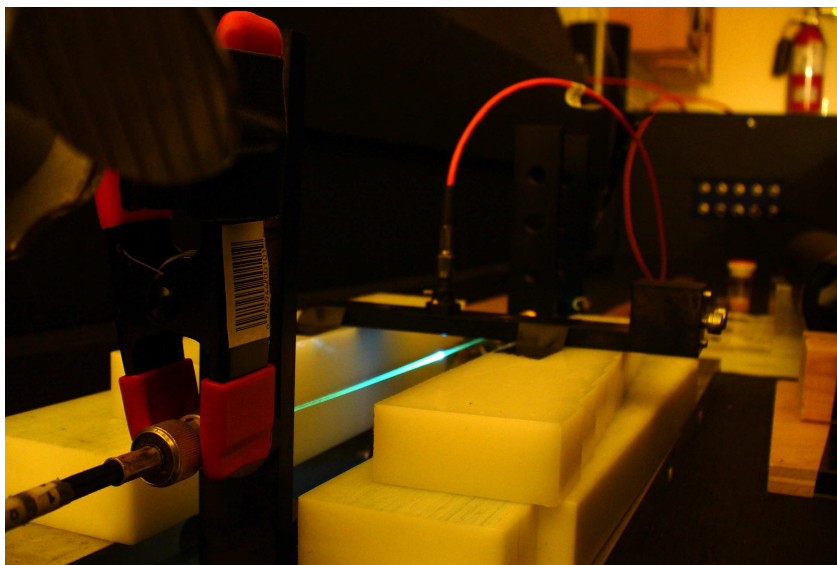
<sup>5</sup>FiberFin 4 Diamond Finish Machine

<sup>6</sup>LeCroy Model 2249A ADC

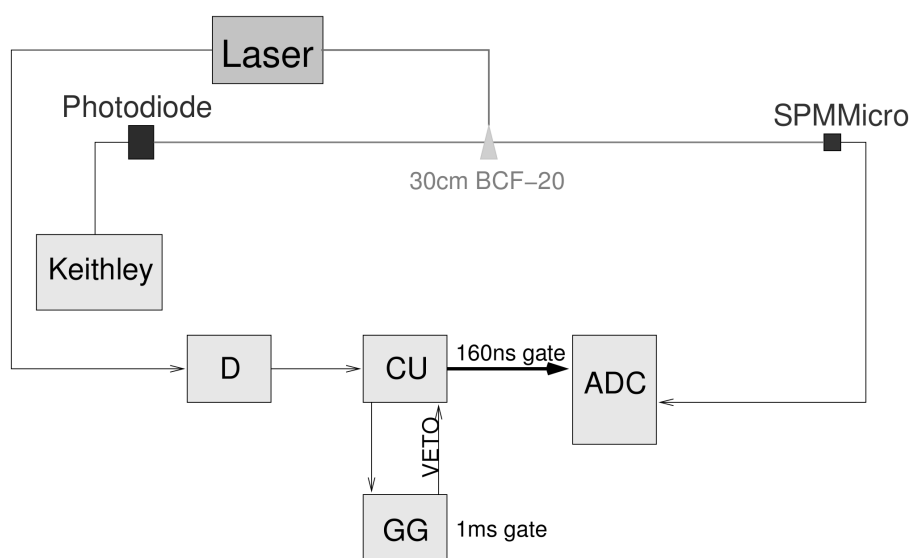
<sup>7</sup>Phillips Scientific Model 705 Octal Discriminator

<sup>8</sup>LeCroy Model 465 Coincidence Unit

<sup>9</sup>LeCroy Model 222 Dual Gate Generator



(a)



(b)

Figure 5.10: Views of the experimental setup for SPMMicro PDE tests including (a) a photograph of the laser illuminating the green scintillating fibre at its centre (original in colour) and (b) a schematic diagram of the setup.

For these particular measurements, the laser's lowest internally controlled repetition frequency of 2.5 MHz was used. While high laser pulse frequencies can result in a baseline offset, as seen in Figure 5.6(b) on page 55, lower frequencies, on the other hand, lead to photodiode currents which are too small to be easily measured. To balance out these two factors, a laser pulse frequency of 2.5 MHz was used for these particular measurements and, since baseline offsets are only observable at 2.5 MHz if large numbers of photons are present in each pulse, care was taken to account for the offsets for higher light intensities where the effects are noticeable.

### 5.2.3.2 Measurements and Analysis

Each PDE measurement involved readings using a number of laser intensities ranging from 2.20 to 2.88. For each intensity, the photodiode current was recorded as the average of 100 readings from the Keithley, and roughly 100,000 events were collected in the ADC spectrum of the SPMMicro. All measurements were taken at a room temperature of around 25°C.

To determine the number of photons in a given laser pulse from the output current of the calibrated photodiode, the effective quantum efficiency of the photodiode must first be determined. This can be done by comparing the photodiode's known quantum efficiency, as a function of wavelength, with the light emission spectrum from a fibre, measured using an Ocean Optics SD2000 fibre optic spectro-photometer [33]. This spectrum changes with distance of the light source from the end of the fibre. For a distance of 15 cm (corresponding to a total fibre length of 30 cm) this comparison can be seen in Figure 5.11, which reveals that for the spectrum emerging from a BCF-20 fast green scintillating fibre illuminated 15 cm from its end, the photodiode quantum efficiency is relatively constant at 67%, which corresponds to a photo sensitivity of 270 mA/W. This information was used to calculate the number of photons incident

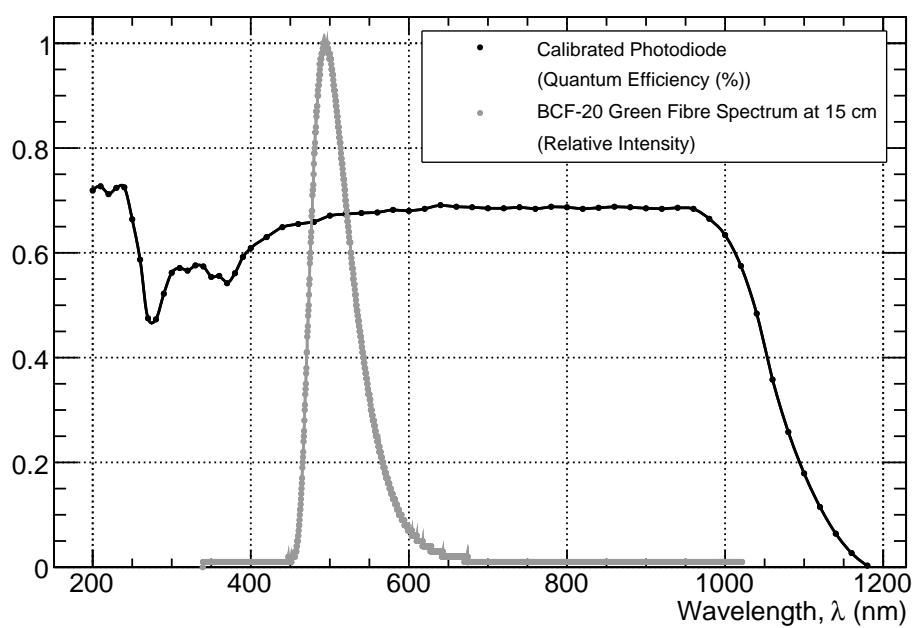


Figure 5.11: This plot shows the quantum efficiency of the calibrated photodiode with respect to the relative intensity of the spectrum emerging from a BCF-20 fast green scintillating fibre illuminated 15 cm from its end.

on the photodiode (and therefore incident on the SPMMicro) based on photodiode current as

$$N_\gamma = \frac{I}{E_\gamma S_\lambda f} \quad (5.3)$$

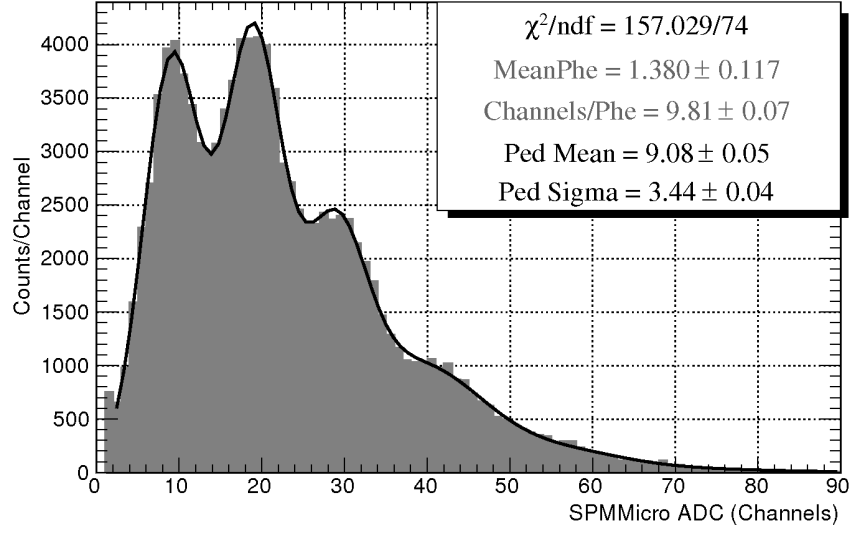
where  $I$  is the photodiode current,  $E_\gamma$  is the energy of a photon of wavelength 500 nm,  $S_\lambda$  is the photo sensitivity of the photodiode at 500 nm, and  $f$  is the frequency of the laser pulses.

For low laser intensities (2.20 to 2.40), individual photoelectron peaks were visible in the SPMMicro ADC spectra. The number of photoelectrons (or number of pixels fired in the SPMMicro) was then extracted by fitting each peak and taking a weighted average of all peaks visible in the spectrum. The pedestal or first peak in the spectra corresponds to zero photoelectrons, the next peak to one photoelectron, and so on (see Figure 5.12(a)). These spectra are convenient because the pedestal position is easy to identify and the distance between photoelectron peaks can be measured, thus calibrating the ADC scale for higher intensities where individual peaks are not visible.

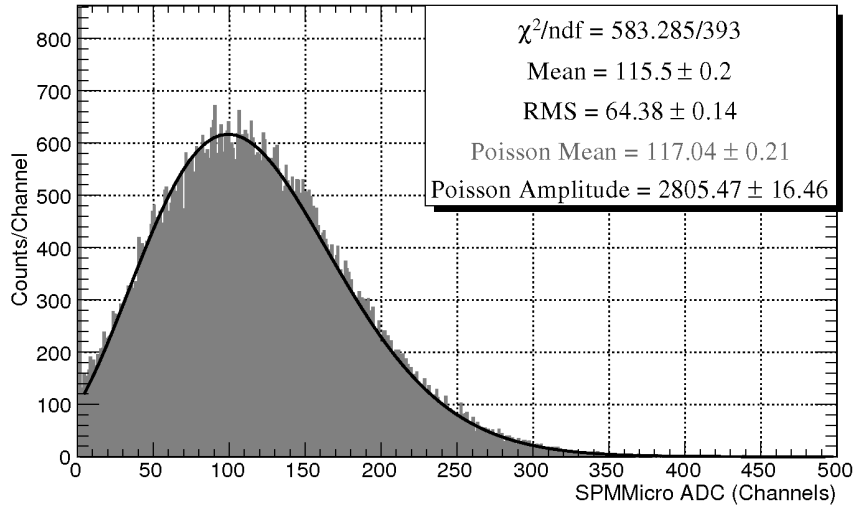
At higher intensities (greater than 2.40), where individual photoelectron peaks were not visible, the number of photoelectrons can be determined as

$$N_{Phe} = \frac{ADC_{Mean} - ADC_{Pedestal}}{Channels/Phe} \quad (5.4)$$

where the  $ADC_{Mean}$  value is determined by fitting the spectra with a Poisson distribution, the ADC-channels-to-Number-of-Photoelectrons factor  $Channels/Phe$  is determined from low intensity spectra, and  $ADC_{Pedestal}$  is the mean value (position) of the zero photoelectron peak (see Figure 5.12(b)). This reflects that the distance between any two successive photoelectron peaks should be the same (since any pixel avalanche results in a similar output current). Assuming the “zero” photoelectron



(a) Laser Intensity Setting 2.30



(b) Laser Intensity Setting 2.80

Figure 5.12: Sample ADC spectra for 3-mm A20HD-07 SPMMicro at (a) low laser intensity where individual peaks are visible, and (b) high laser intensity where peaks are not visible. Note that in plot (b) the pedestal has clearly shifted to a lower value than in (a), as there is a build-up of events in ADC channel zero.

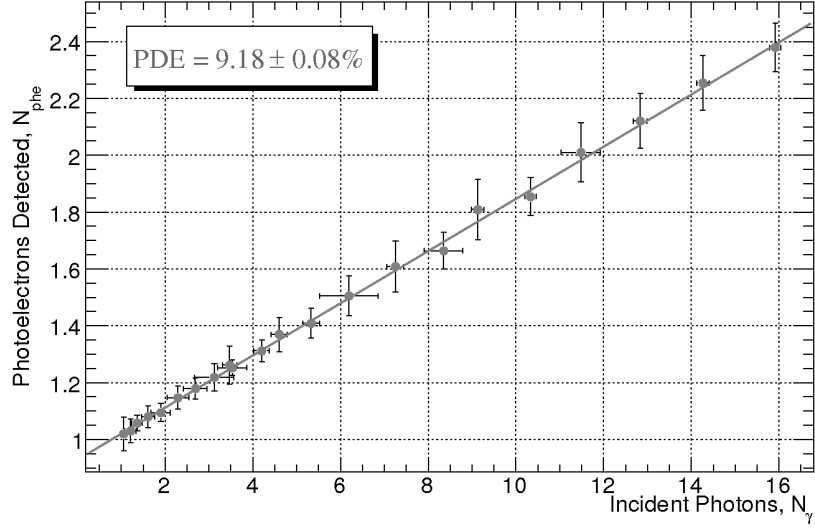
peak (or pedestal) is in the same position, even at high light intensities where individual peaks are not distinguishable, the number of photoelectrons present in any spectrum can be determined; however, this pedestal position shifts to the negative ADC scale with increased intensity, as described above in Section 5.2.2.1 and seen in Figure 5.12(b). By observing signals on an oscilloscope, the baseline offset was estimated and the expected pedestal shift was calculated via Equation 5.2. This information was then used to extract the number of photoelectrons in the spectra.

The slope of a graph of photoelectrons detected by the SPMMicro versus incident photons gives an accurate measurement of a SPMMicro's PDE, assuming a linear fit of the data. The intercept of such a graph is representative of the dark current of that SPMMicro as it estimates the leakage current, or noise, in the absence of light.

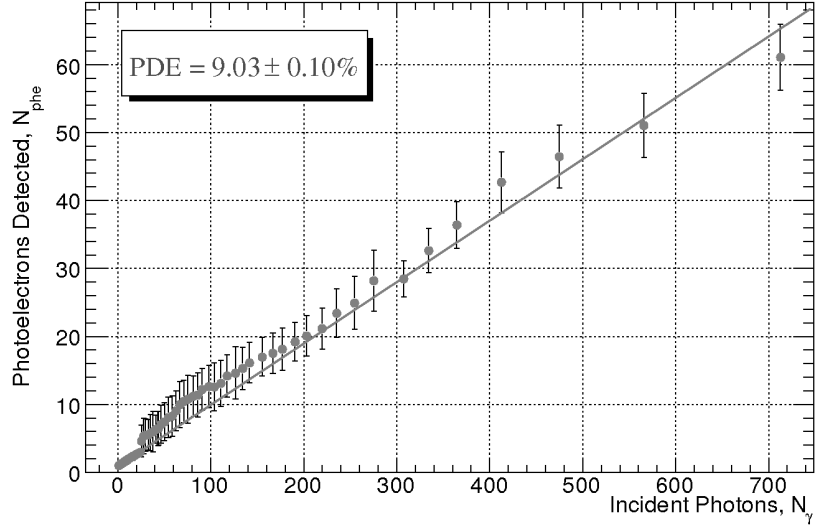
Looking only at low intensity spectra, where individual photoelectron peaks are visible, a simple graph of the number of photoelectrons (from the SPMMicro ADC) versus the number of incident photons (from the photodiode current) shows the PDE of the SPMMicro at overbias +3.0 V and gate duration 160 ns to be  $9.18 \pm 0.08\%$  (see Figure 5.13(a)). When high intensity data are included, the PDE is  $9.03 \pm 0.10\%$  which is consistent with low intensity results (see Figure 5.13(b)), but because of the added uncertainties introduced with the high intensity method of photoelectron calculation, these data clearly do not strictly follow the linear relation established by low intensity data.

Repeating these measurements for different overbiases and gate widths gives an impression of the effect these parameters have on SPMMicro PDE. Figure 5.14(a) on page 70 shows PDE measurements at overbiases of +2.0 V, +2.5 V, and +3.0 V. As expected, the PDE increases slightly with increased overbias, although this is offset by a corresponding increase in the intercept, which represents dark current.

Figure 5.14(b) on page 70 shows PDE measurements at two different gate widths,



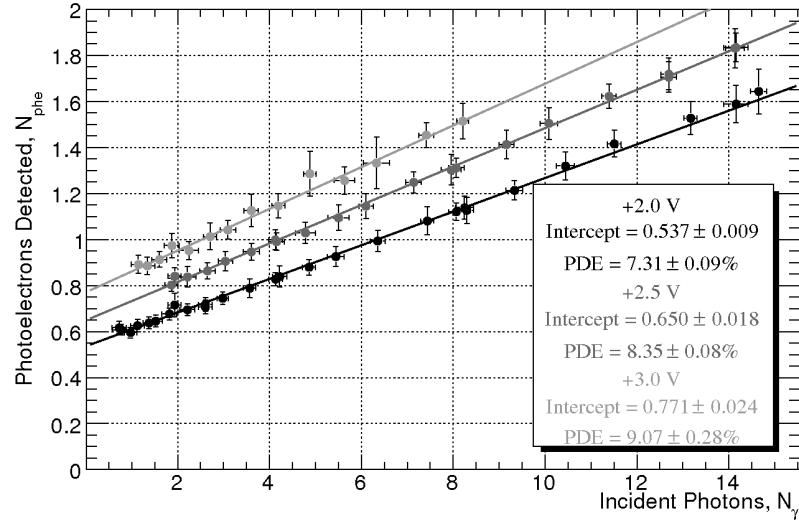
(a) Low Intensity Data



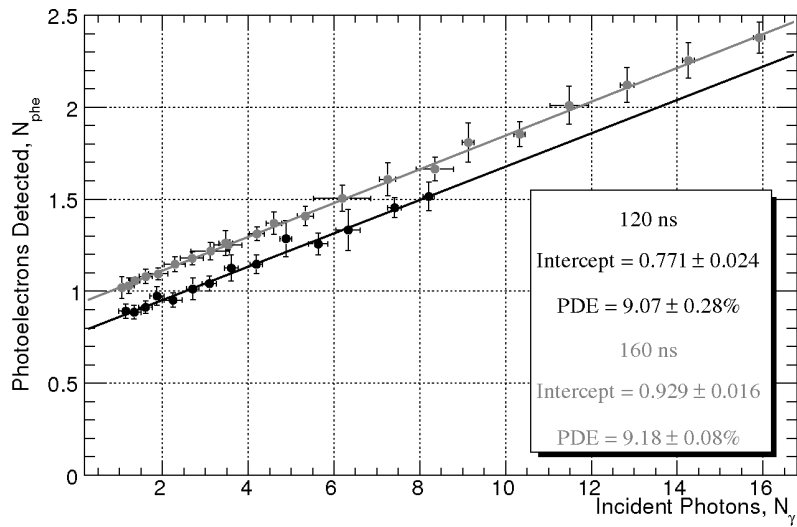
(b) Low and High Intensity Data

Figure 5.13: SPMMicro 3-mm A20HD PDE at overbias +3.0 V, gate duration 160 ns and laser frequency 2.5 MHz. In plot (a) only low intensity data are shown, while in plot (b) both low and the pedestal-corrected high intensity data are included.





(a) Variable Overbias; Constant Gate Width



(b) Variable Gate Width; Constant Overbias

Figure 5.14: SPMMicro 3-mm A20HD-07 PDE at (a) overbiases of +2.0 V, +2.5 V and +3.0 V, laser frequency 2.5 MHz, and ADC gate width 120 ns, and (b) ADC gate widths of 120 ns and 160 ns, laser frequency 2.5 MHz, and overbias +3.0 V. For each PDE measurement, data are presented only for the laser intensities where individual photoelectron peaks were visible.

but at the same overbias. Lengthening the gate width does not visibly affect PDE, but as expected for any device with non-zero noise in its signal baseline, this does result in an increased intercept.

PDE measurements of 1-mm A20HD and 1-mm A35HD devices were made at overbiases of +2.0 V, +2.5 V, and +3.0 V (see Figure 5.15), but the lack of resolution of individual photoelectron peaks at room temperature precluded measurements of 3-mm A35HD devices. All results are summarized in Table 5.2. Based on results for 3-mm A20HD devices, PDE values can be projected for 3-mm A35HD devices, assuming PDE scales up from A20HD to A35HD devices for the 3-mm geometry the same way it does for the 1-mm geometry; however, in projected PDE values for 3-mm A35HD devices, the excessive noise at room temperature is not taken into account.

Based on results for 3-mm A20HD devices, and assuming PDE scales up from A20HD to A35HD devices for the 3-mm geometry the same way it does for the 1-mm geometry, the PDE of 3-mm A35HD devices is estimated to be between 12 and 13%.

Referring to Section 4.2.3, there is no reason for the PDE of 1-mm devices to be substantially lower than 3-mm devices. PDE depends only on the quantum efficiency of the silicon, the geometric fill factor, and the probability of a photon initiating a Geiger-mode discharge in a pixel - all factors which should be constant for both 1-mm and 3-mm devices. The difference here is rooted in the coupling of a scintillating fibre to a SPMMicro. Considering that the scintillation light must pass through a layer of protective glass and an air gap between the glass and silicon of each SPMMicro device, it can be calculated that the final light profile incident on the SPMMicro active area has a radius of roughly 1.28 mm. For 3-mm devices, this entire profile falls on the active area of the SPMMicro, but for 1-mm devices, only about 20% of this light is intercepted by the device. If 1-mm devices were to view all of the scintillation light from the scintillating fibre, they should have the same PDE as 3-mm devices.

Table 5.2: PDE values for SPMMicros as determined in Regina.

Overbias (V)	PDE (%)		
	3-mm A20HD	1-mm A20HD	1-mm A35HD
+2.0	$7.31 \pm 0.09$	$1.99 \pm 0.11$	$3.47 \pm 0.09$
+2.5	$8.35 \pm 0.08$	$2.64 \pm 0.03$	$3.93 \pm 0.04$
+3.0	$9.07 \pm 0.28$	$3.32 \pm 0.07$	$4.47 \pm 0.03$

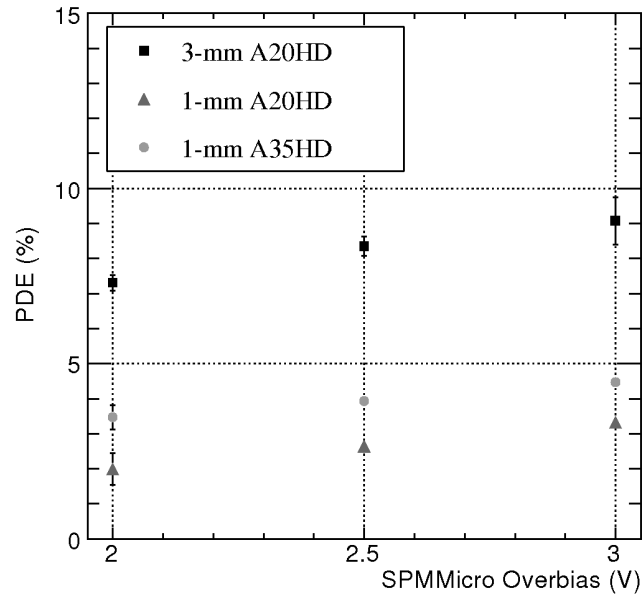


Figure 5.15: Measured PDE values for 1-mm A20HD and A35HD and 3-mm A20HD SPMMicros.

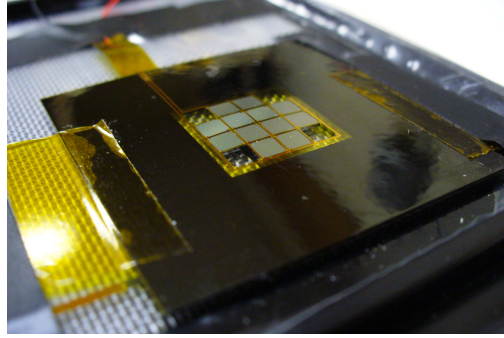
### 5.3 SensL SiPM Arrays

SensL's development of large area SiPM arrays over the past few years has been a multi-step process. The GlueX collaboration requested that new prototype models of large area SiPMs be delivered for testing either to JLab or to the University of Regina. Results from tests performed using these prototype arrays have provided valuable feedback not only on the functionality of the arrays in general, but also on the suitability of these devices to the GlueX BCAL readout.

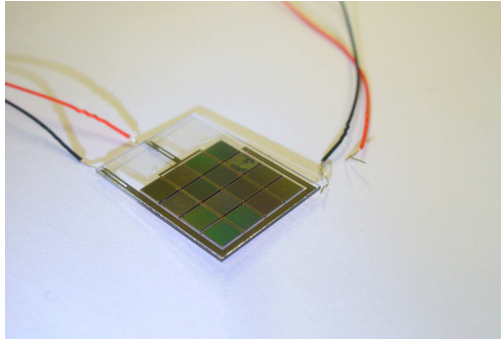
The SensL SiPM arrays are each composed of 16 3-mm SiPM devices arranged in a  $4 \times 4$  matrix, giving the total array an active area of  $1.2 \times 1.2 \text{ cm}^2$ . As the silicon is treated the same whether it is to be used in a SiPM array or a SPMMicro, each element of the array is essentially one 3-mm SPMMicro. Current output from each of the 16 elements is summed into one output for each array. The general quality of the arrays delivered to Regina improved significantly with each new prototype, to the point where, in 2009, SensL offered the first large area SiPM devices to be available commercially.

All SiPM arrays tested in Regina can be seen in Figure 5.16. These prototype arrays arrived in Regina beginning in August 2007 and ending in December 2008. In chronological order, these are individual 12-cell flex-mounted and 16-cell glass-mounted arrays, a set of four additional glass-mounted arrays (G-series), a SPMPlus array, and a set of five SPMP arrays.

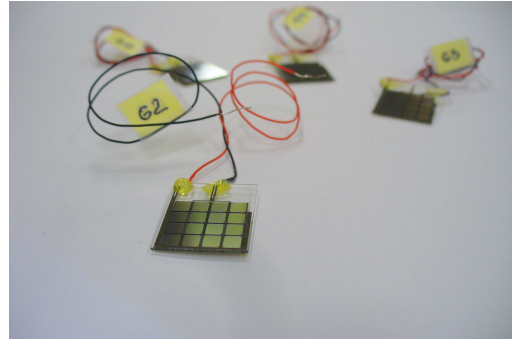
The original SiPM array delivered to Regina was a flex-mounted device with the silicon applied directly to a flexible plastic surface. A subsequent prototype, along with four additional arrays, had the silicon applied to a glass surface. The flex-mounted and glass-mounted arrays each had two loose wire connectors that were meant to connect the SiPM array to an electronic board (powered by external power supplies, as with SPMMicros). Those wires were difficult to work with and had a



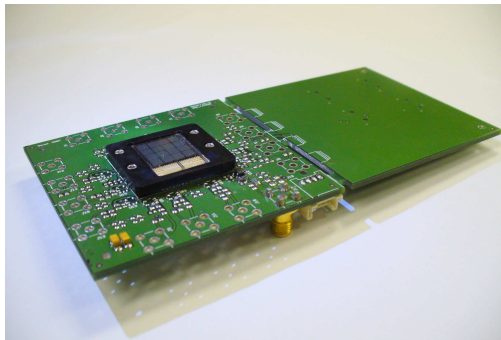
(a) Flex-mounted array



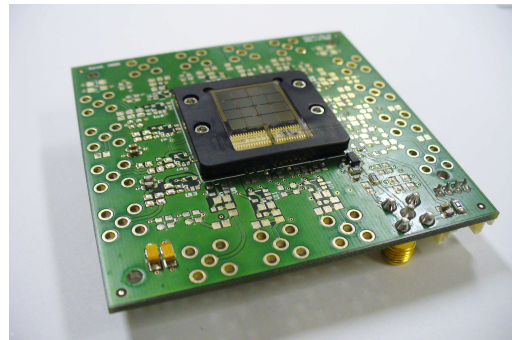
(b) Glass-mounted array



(c) G-series arrays



(d) SPMPlus



(e) SPMP

Figure 5.16: Photographs of SensL SiPM arrays that were tested in Regina (original in colour).

tendency to detach from the detectors with repeated use.

The first SPMPlus array (see Figure 5.16(d)) incorporated improvements both in the silicon processing, as well as in the electromechanical connections and packaging, as compared to the glass-mounted arrays. Finally, the performance of SPMP arrays exhibited evidence of improved electronics as well as better gain uniformity than earlier SensL arrays.

For the SPMPlus and SPMP arrays, contact to electronic boards was made through pin connections. Each array came attached to its own electronic board (equipped with a four-way power cable connector and an SMA signal output) and did not need to be disconnected. Also, for the SPMPlus and SPMP arrays, power was delivered through a power board which snapped into place onto the electronic board. Through an adapter, this power board plugged into any electric wall receptacle, and was preset to deliver a bias voltage of +2.0 V (based on  $V_{br}$  measurements made at SensL) as well as appropriate amplifier voltages. The bias voltage delivered could be adjusted by a potentiometer on the power board [31]. The option of bypassing the power board entirely and supplying power to the electronic board with external power supplies was also available.

While the addition of attached electronic boards increased the space required for each array significantly, the packaging size was cut roughly in half from the SPMPlus array to SPMP arrays. Those two types of arrays were for testing only and made no claim to be in the compact configuration required for application to the BCAL readout.

### 5.3.1 IV Characterization

Using the Keithley Picoammeter/Voltage Supply, IV characteristics were mapped out for SiPM arrays using the same method used for SPMMicros. For the flex-mounted

and glass-mounted arrays, the two connecting wires were treated as the cathode and anode pins on an individual SPMMicro housing when performing IV sweeps. For SPMP arrays (where the array was mounted to an electronic board), the blue (bias) and black (ground) wires on a four-way colour-coded power cable were used. While that method did not allow for isolation of the array from its electronics, an accurate picture of the dark current and IV characteristic could be obtained, provided the amplifier was not powered.

Because arrays are composed of 16 individual SiPM elements, it is possible for some elements to have a different breakdown voltage than others. If this is the case, it would be evidenced by the appearance of multiple breakdown regions on an IV curve. This is problematic because bias voltage can only be applied to the array as a whole, not to individual elements, which would result in different elements being operated at different overbiases. Inconsistent breakdown voltages across the array did not appear to be an issue for SensL arrays tested in Regina.

Representative IV characteristics for the three types of arrays (flex-mounted, glass-mounted, and electronics-coupled) can be seen in Figure 5.17, where it should be noted that the dark current was reduced by a factor of roughly 200 from the flex-mount to the first glass-mounted array. The dark current for all other SensL SiPM arrays is slightly, but not significantly, higher than that of the first glass-mounted array. From these IV characteristics, breakdown voltages were determined for individual arrays (see Table 5.3).

### 5.3.2 Gain Uniformity

To measure gain uniformity across an array, each individual cell's response must be measured when exposed to the same source of light. These measurements can then be compared to one another.

Table 5.3: SiPM array breakdown voltages as determined in Regina. Values marked with an asterisk (\*) are specified by SensL.

Array Type	ID	$V_{br}$ (V)
Flex-mount	-	27.05
Glass-mount	-	27.60
G-Series	G2	27.20
	G3	27.20
	G4	27.20
	G6	27.25
SPMPlus	-	28.30*
SPMP	2	27.10
	10	26.80
	11	28.10
	13	27.50
	15	28.20

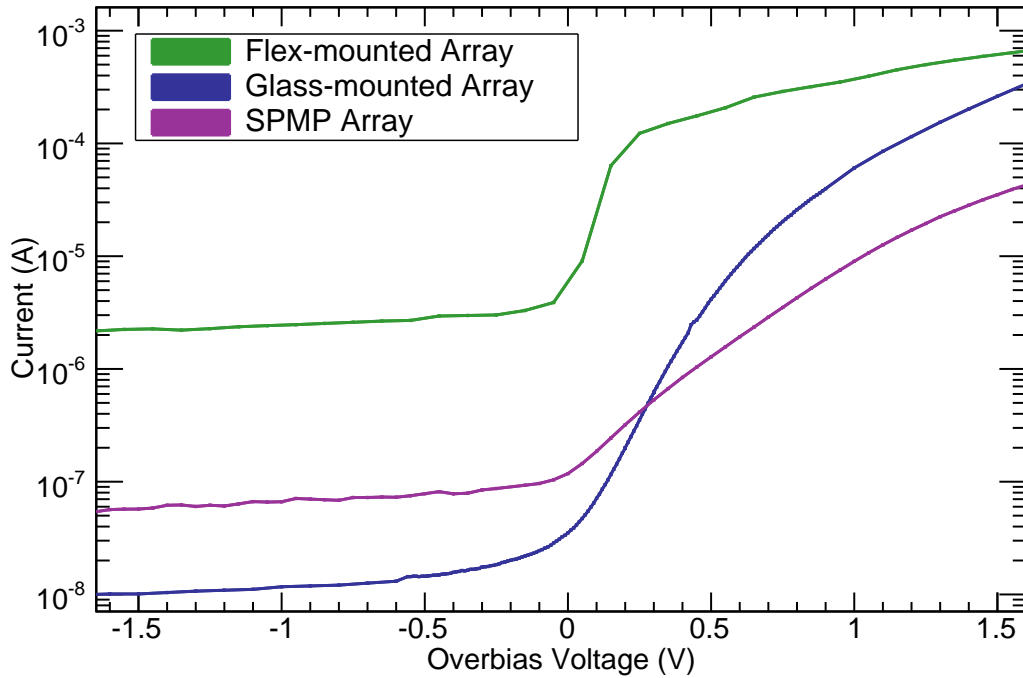


Figure 5.17: IV characteristics of SensL SiPM arrays (original in colour).



For all gain uniformity tests designed and carried out in Regina, the response of each cell of an array was measured by observing resulting signals on the Tektronix oscilloscope. Attaching an SMA-to-BNC adapter to the SMA output of the electronic board for the array, and using a 1.5 m long RG-58 coaxial cable, signals were sent to the oscilloscope. As light was applied to an individual cell, the amplitude of the array's signal output was measured on the oscilloscope (in mV) and signal amplitudes were averaged over 30 seconds. Since light was only applied to one cell while the other 15 cells were "dark", this average signal amplitude represented the response of the single "lit" cell.

Gain uniformity results presented in this section have all been normalized relative to the maximum amplitude of any cell in an individual array. While signal amplitude varied from array to array, the purpose of those measurements was to establish the level of gain uniformity across individual arrays. The convention for labeling cells in an array is established in Figure 5.18.

To apply light to cells in an array, the PicoQuant laser was used at relatively high intensity. The pulses coming from the fibre output of the laser had a repetition frequency of 2.5 MHz, and a pulse width of approximately 60 ps. These pulses passed through one coupling point (laser to scintillating fibre) and through a scintillating fibre approximately 30 cm long<sup>10</sup>, with SMA connectors attached on each end, before illuminating the SPMPlus. With a 60 ps laser pulse duration, the resultant pulse width from the scintillating fibre is roughly 5 ns due to the intrinsic time structure of the fibre.

The main logistical challenge with these measurements is ensuring that only one cell of the array is exposed to light. The original gain uniformity test, performed on the first glass-mounted array, was exceedingly simplistic. A mask was made with

---

<sup>10</sup>Saint-Gobain BCF-20 Fast Green Scintillator

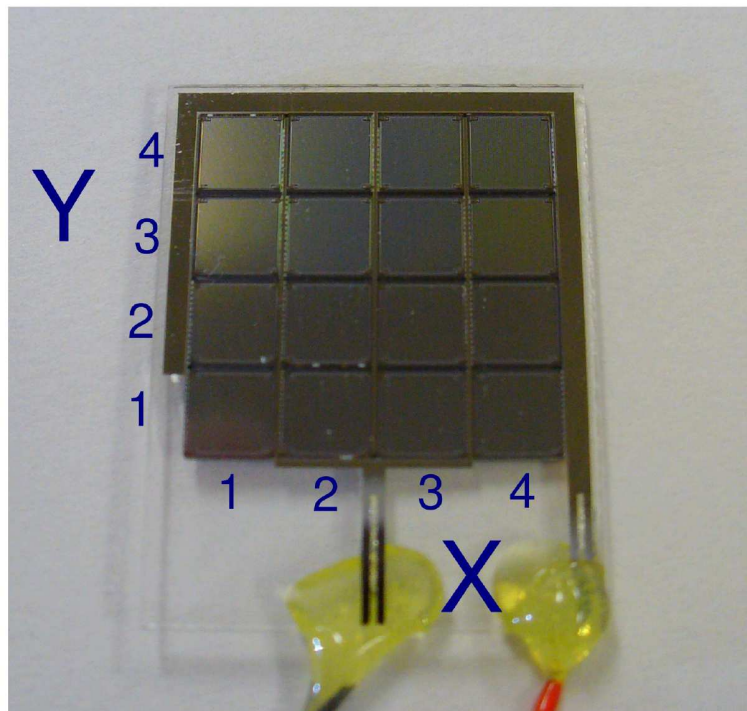


Figure 5.18: An image of a glass-mounted array illustrating the orientation of the x- and y-axes on the array (original in colour). The electrical connections are at the bottom of the array in this picture. This labeling convention is used for cells in all arrays.

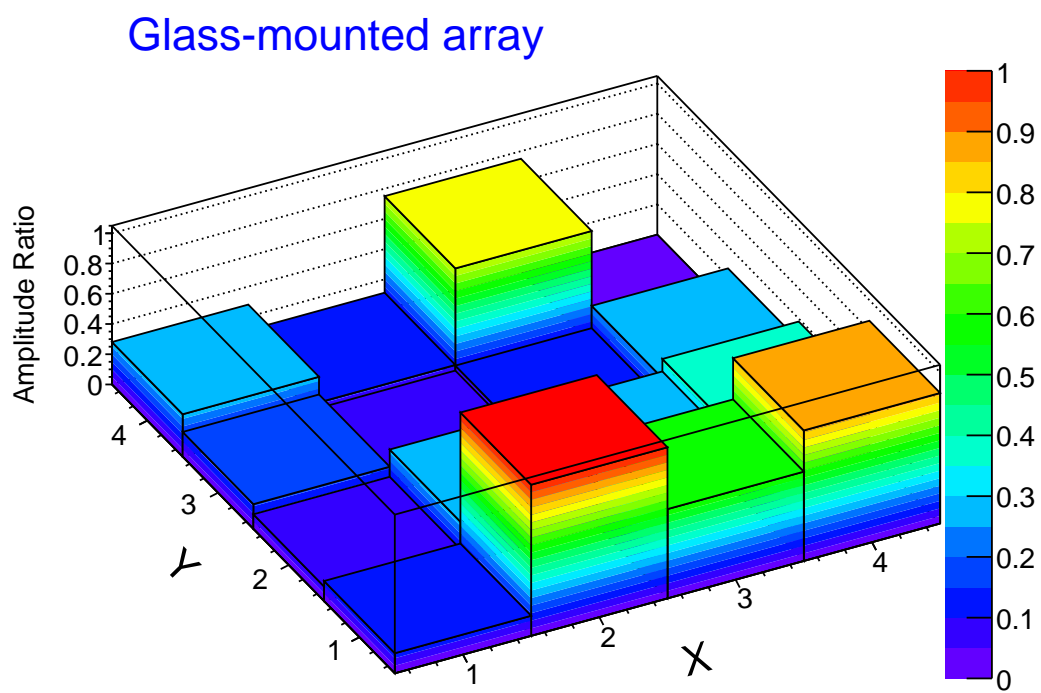


Figure 5.19: Amplitude ratio measurement of the first SensL glass-mounted array (original in colour).

a microscope slide and black tape which covered the entire array, leaving only one cell exposed. Working in a dark room, light was applied by the scintillating fibre, held by hand against the exposed section of the mask. The mask was then moved around to test each cell in turn. Results from this original measurement can be seen in Figure 5.19. On average, the amplitude deviation of any cell from the average amplitude of the array as a whole is  $24 \pm 16\%$ , with a maximum deviation of 63% - significantly worse than the 10% gain uniformity specified by the GlueX collaboration.

With the arrival of the set of G-series glass-mounted arrays, a more reliable method of applying light to individual cells was sought. A device was designed to ensure reproducible light application for glass-mounted arrays (a photograph of the device can be seen in Figure 5.20(a)). A glass-mounted array slid into the device where its cells were aligned with 16 holes. Each hole had a wide section, allowing for the placement and secure alignment of the scintillating fibre's SMA connector, and a 5 mm long, 1 mm diameter section, which collimated the light before it was intercepted by the cell (see Figure 5.20(b)). Gain uniformity results for the G-series glass-mounted arrays, measured using this apparatus, can be seen in Figure 5.21. For each of these devices, the average amplitude deviation of any cell from the average amplitude of the array was around  $13 \pm 10\%$ , with a maximum deviation between 20 and 30%. Measurements were only completed for three of the four G-series arrays in Regina. Damage to the electrical contacts for array G4 rendered it unusable, and further verified the need for more robust SiPM array packaging.

Improvements to the SiPM array packaging were matched by improvements in the method used to illuminate individual cells of an array. A stand was built to accommodate a movable x-y stage<sup>11</sup> and to hold the output fibre from the laser head (see Figure 5.22(a) on page 84). The fibre output from the laser was connected to the

---

<sup>11</sup>Two Zaber T-LS Series Motorized Linear Stages connected for movement in two dimensions.

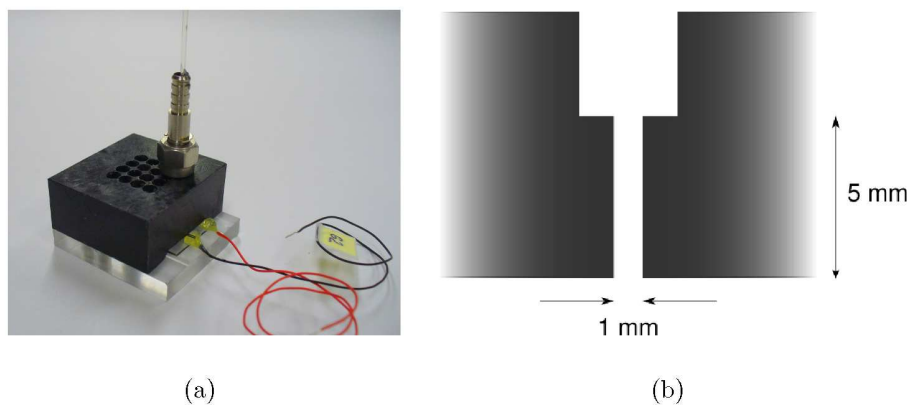


Figure 5.20: (a) Picture of the experimental apparatus built in Regina for gain uniformity testing of G-series glass-mounted arrays (original in colour), along with (b) a cross-sectional sketch of a single hole in the apparatus.

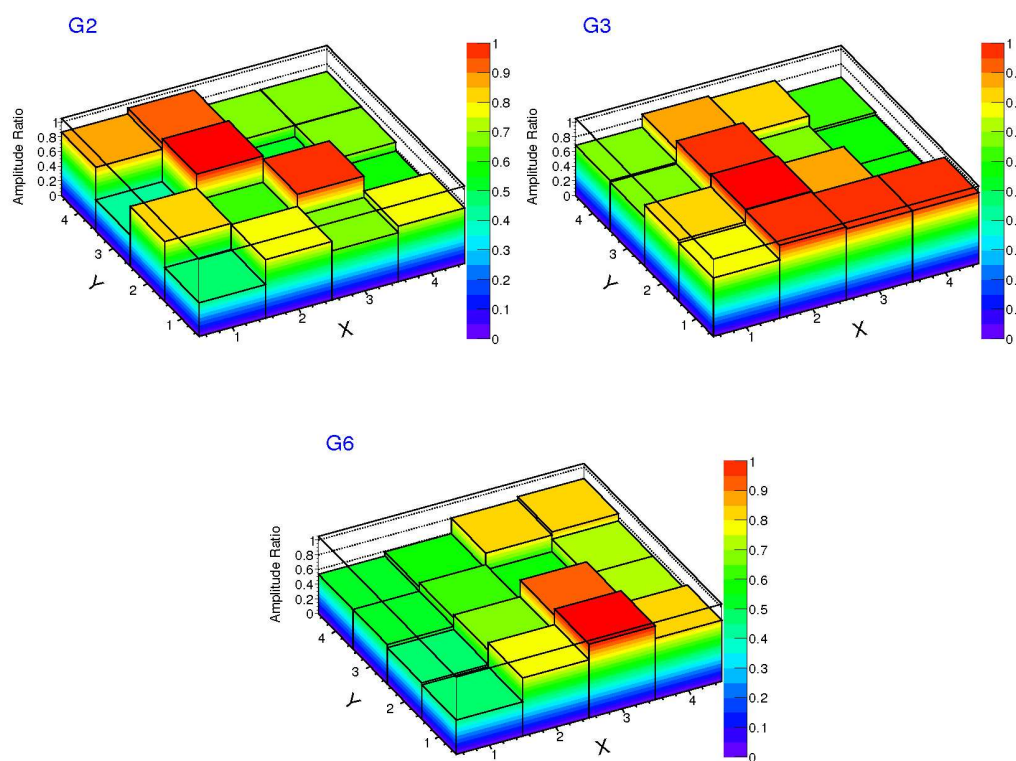


Figure 5.21: The average amplitude ratios for G-series glass-mounted arrays (original in colour).

scintillating fibre with an SMA-to-SMA barrel connector built into the top support on the stand. The other end of the scintillating fibre was connected to the bottom support where a 1.48 cm long collimator with an aperture of 1-mm diameter was located (see Figure 5.22(b)). SiPM arrays attached to electronic boards (SPMPlus and SPMP arrays) were mounted on the x-y stage using four screws, allowing the array to be moved around in two dimensions while the stationary fibre illuminated a 1-mm diameter spot on any cell in the array. The position of the x-y stage was controlled using software provided by Zaber and modified for gain uniformity testing in Regina. The x-y stage has precision on the order of microns. This setup allowed not only for repeatable precision alignment of a collimated light source on the centre of each cell in an array, but also for the scanning of individual cells to determine the uniformity across the entire surface of one array element.

The entire SPMPlus array was scanned ten times, applying light at the centre of each cell. A surface plot constructed using the average of these ten measurements for each cell can be seen in Figure 5.23(a). The average amplitude deviation was  $24 \pm 17\%$  with a maximum deviation of 64%. If the particularly low-functioning cells ((1, 4), (2, 1), (3, 1), and (4, 2)) are ignored in the analysis, the average deviation is  $7 \pm 4\%$  with a maximum deviation of 15% for the remaining cells, giving a picture of the gain uniformity across the functional cells of the array. Some early measurements for cells (1, 4), (2, 4), (3, 4), and (4, 1) gave amplitudes very different from subsequent measurements. This behaviour was limited to the first four measurements taken of the array, and is believed to be linked to intermittent electrical connections. Clearly anomalous results were excluded for each individual cell, and after this the standard deviation over ten independent measurements was about one or two per cent in each case.

Concerns regarding the electronics accompanying the first SPMPlus led to the

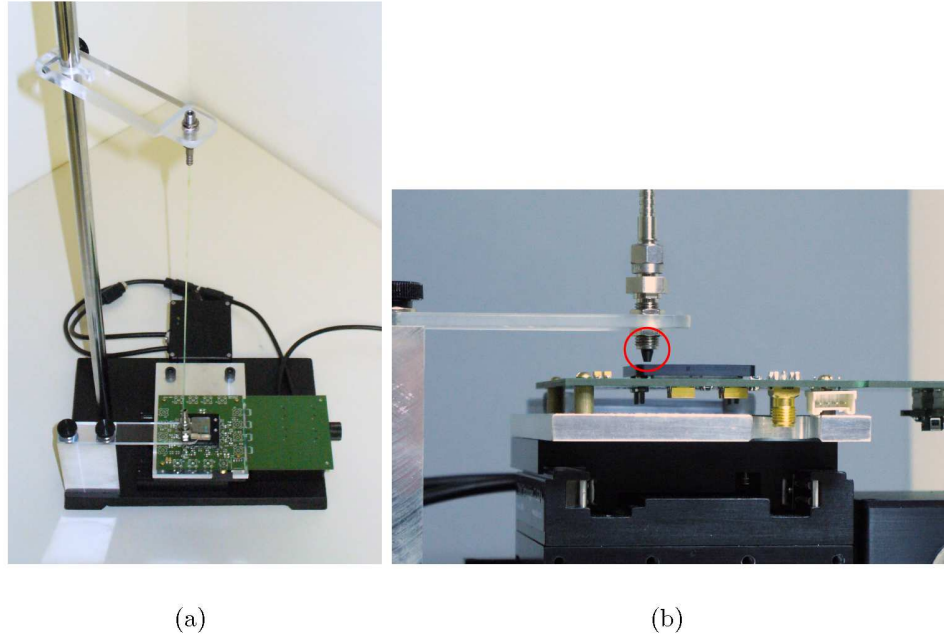


Figure 5.22: Pictures of the experimental apparatus built in Regina for gain uniformity testing of SensL SPMPlus and SPMPs (original in colour). Note the black tapered collimator protruding from the bottom connection point, circled for clarity.

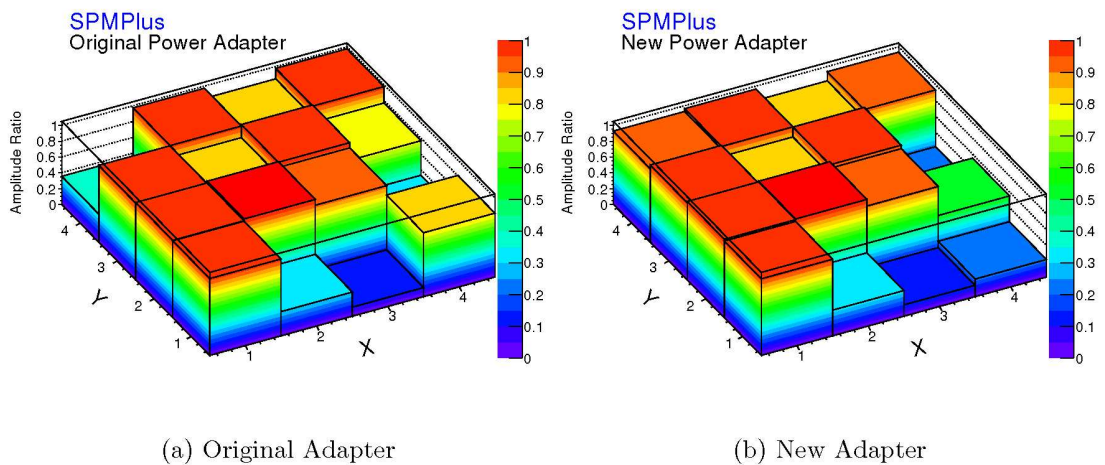


Figure 5.23: The average amplitude ratios for individual cells of the first SensL SPM-Plus (original in colour). In both cases, each cell is compared to cell  $(x, y) = (2, 2)$  which consistently had the maximum gain for the array.

procurement of an additional power adapter from SensL. Identical measurements of the gain uniformity of the SPMPPlus were taken with the new adapter (see results in Figure 5.23(b)). The “resurrection” of cell (1, 4), and the “death” of cells (4, 1) and (4, 3) indicate that electrical connections are indeed intermittent, meaning that the gain non-uniformities observed are not necessarily indicative of problems with the silicon in those elements of the array.

As a final test, the gain uniformity of individual cells within the SPMPPlus was measured. The procedure was similar to that of the gain uniformity tests on the entire array. For these tests, the 1-mm diameter light spot was used to illuminate the lower left-hand corner of a cell (as defined in Figure 5.18 on page 79) and was then moved along the cell in increments of 0.35 mm in the x- and y- directions. A fringe of about 0.5 mm (one radius of the light spot) was left untested around the perimeter of each cell in order to eliminate geometric effects at the edges of the cells. The results of these tests can be seen in Figure 5.24. Comparing Figure 5.24 to Figure 5.23(b), it is notable that well-functioning cells (those with high amplitude ratios) show better uniformity across the cell than poorly-functioning cells (those with low amplitude ratios such as cells (2, 1), (3, 1), (4, 1), (2, 4), and (3, 4)).

Results from gain uniformity measurements taken across each SPMP array, applying light at the centre of each cell, can be seen in Figure 5.25 on page 87. SPMP and SPMPPlus measurements were taken in the same way, but these SPMP arrays show significant improvements in gain uniformity from the SPMPPlus array. Two out of the five arrays (SPMP 2 and 11) exhibit gain uniformity of  $2\pm 2\%$  and  $2\pm 1\%$  and maximum deviations of 6% and 4%, respectively, across the entire array, while the other three arrays (SPMP 10, 13, and 15) each have two cells which appear to be either completely or mostly nonfunctional, with the other 14 cells having gain uniformities of  $2\pm 2\%$ ,  $3\pm 2\%$ , and  $4\pm 2\%$ , respectively, and maximum deviations of less than 8%.



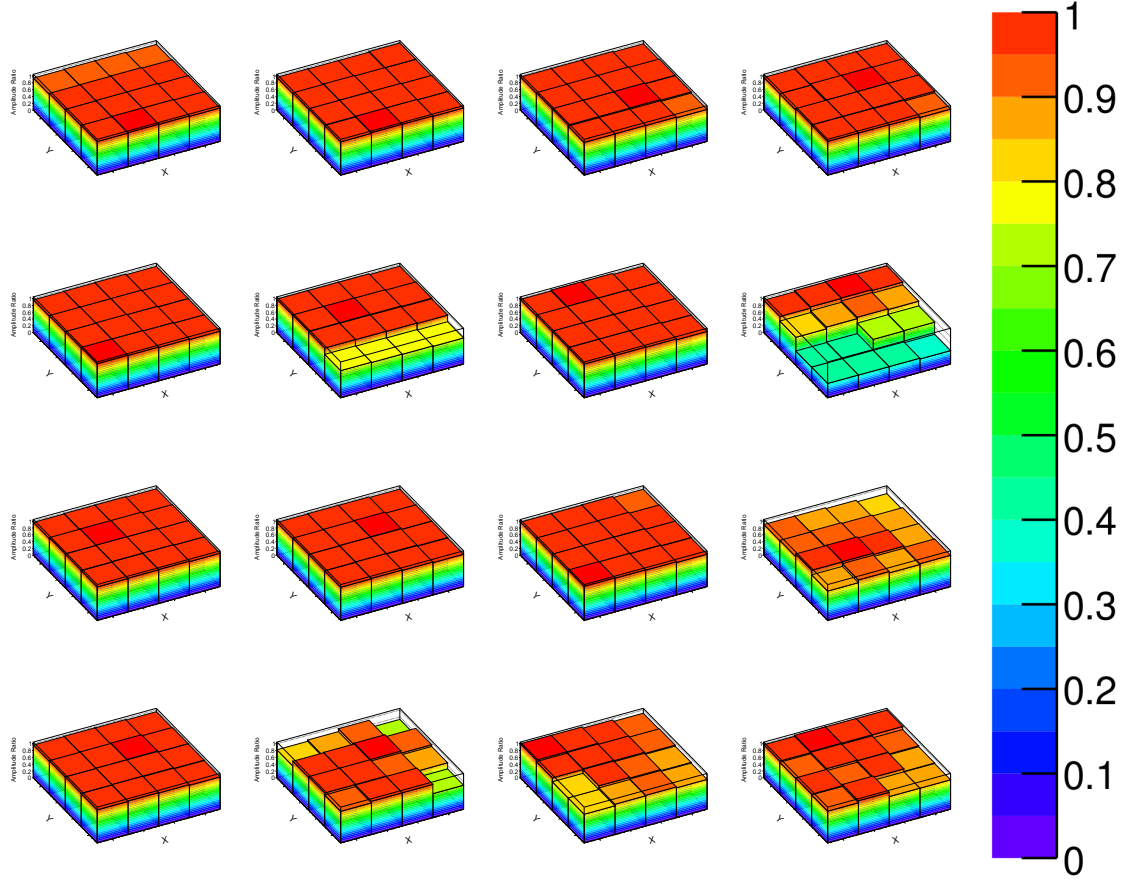


Figure 5.24: The amplitude ratio results of surface scans of each individual cell in the SPMPlus array (original in colour). Orientation of the plots corresponds to Figure 5.18 where the bottom left-hand corner shows results for cell (1, 1) and the top right-hand corner shows results for cell (4, 4). Note that each plot represents a set of independent measurements, and that in each case the measurements were normalized with respect to the maximum amplitude of any measurement for that cell.

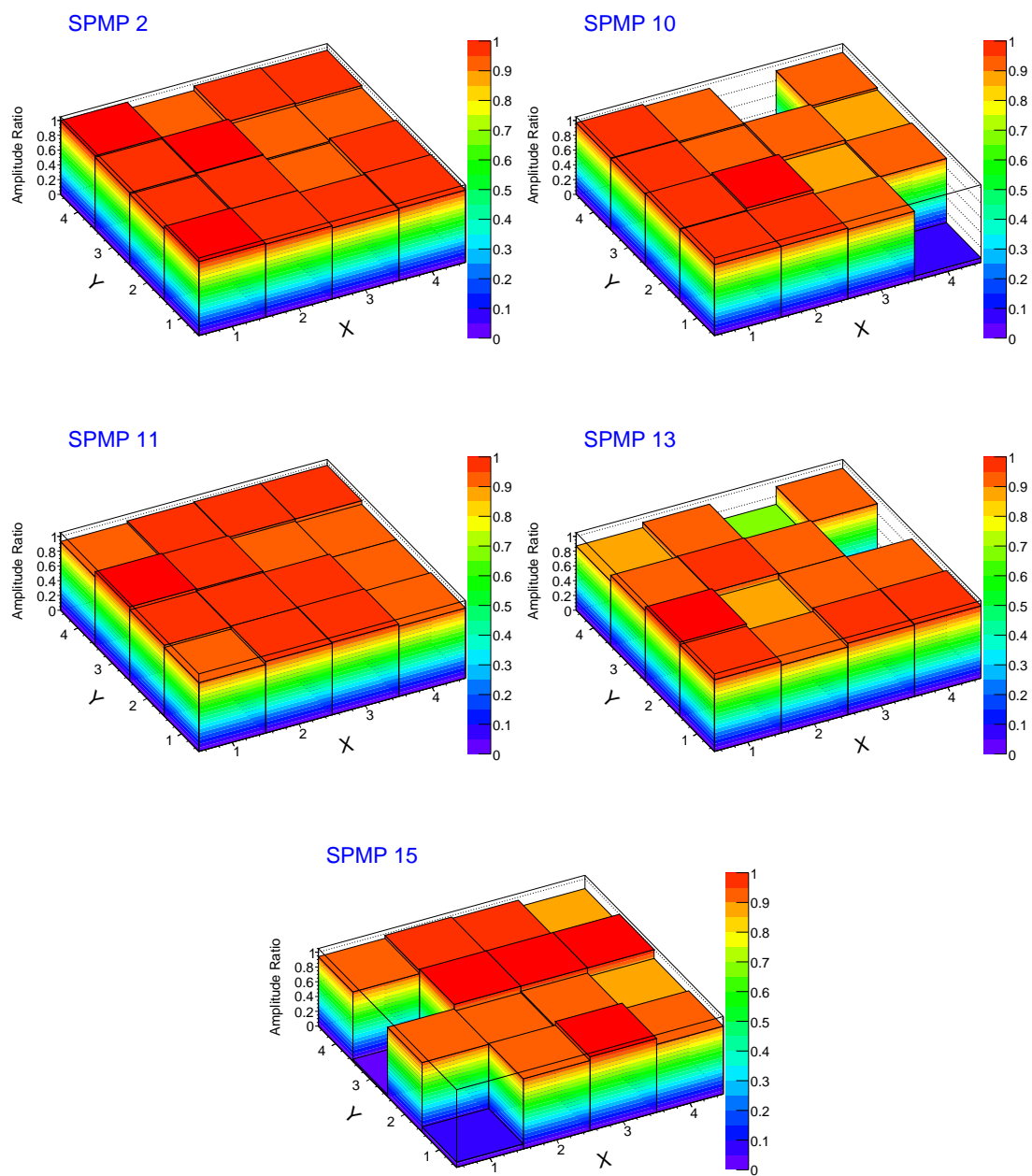


Figure 5.25: The average amplitude ratios for SPMP arrays (original in colour).

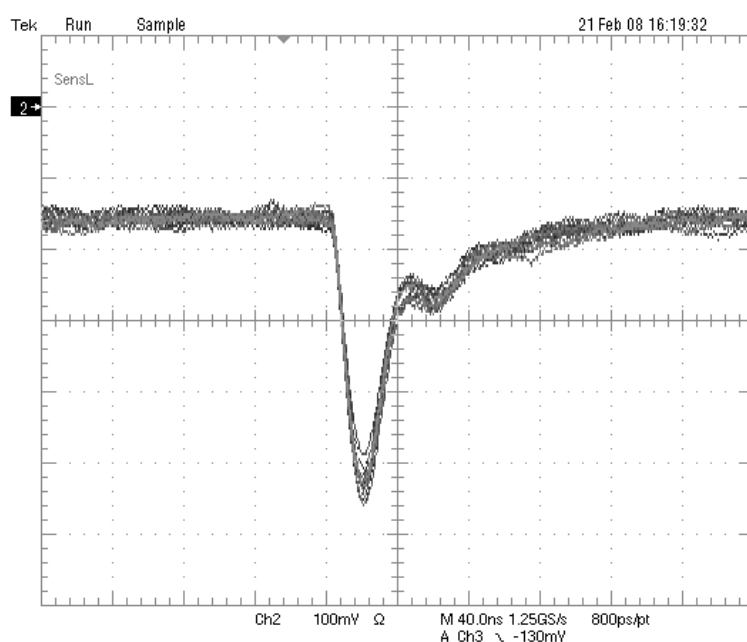


Figure 5.26: Typical signal produced from the SensL SPMPlus. The major scale divisions are 100 mV on the vertical axis and 40 ns on the horizontal axis. As read from the scope, this signal has an amplitude of  $0.375 \pm 0.019$  V, a rise time of  $10.8 \pm 0.4$  ns, and a fall time of  $76.91 \pm 0.14$  ns, although the small reflection seen approximately 40 ns after the initial pulse is increasing the value of the fall time. This is a reflection that is believed to originate somewhere in the setup, and is not indicative of a problem with the SPMPlus. Because the pulses used to illuminate the SPMPlus have a width of only about 5 ns, the source does not account for a significant contribution to the timing of this signal.

### 5.3.3 Signal Analysis

Since the SPMPPlus was the first array with stand-alone electronics (all previous arrays required the use of the same electronic boards used for SPMMicros), an evaluation of signal quality is worthwhile.

A typical SPMPPlus signal can be seen in Figure 5.26. This signal has an offset opposite to the baseline offset observed with the SPMMicro electronic boards. Like the SPMMicro offset, this SPMPPlus baseline offset increases with increased light intensity applied to the array.

Further modified electronic boards accompanied the SPMP arrays. A typical SPMP signal can be seen in Figure 5.27. Again, there is a small baseline offset (approximately 30 mV); however, for these electronics, the baseline shift remains constant for any light intensity, and for any laser pulse rate. The oscillation following the SPMP signal shows that, while these electronics have succeeded in controlling baseline offsets in signals, there is room for further optimization of these electronic boards.

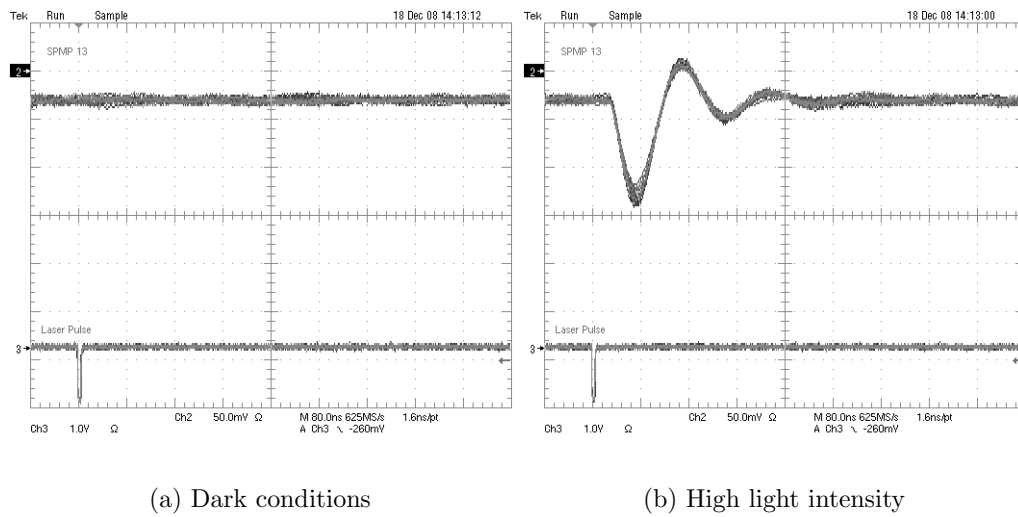


Figure 5.27: Typical signals produced from the SensL SPMP arrays. These scope traces were taken with SPMP 13 with (a) dark conditions and (b) high light intensity applied to the array. In each case, the major scale divisions are 50 mV on the vertical axis and 80 ns on the horizontal axis.

# Chapter 6

## Conclusions



he GlueX collaboration is considering large area SiPMs for use as the readout for the electromagnetic barrel calorimeter. SiPMs have the advantages of immunity to magnetic fields, being more compact than traditional vacuum PMTs, and requiring only low voltage (less than 50 V). Prototype SensL SiPM arrays, along with individual SPMMicro devices, have been researched in Regina in terms of IV characteristics, PDE of SPMMicros, and gain uniformity of SiPM arrays. Qualitative analyses of output signals, individual photoelectron detection capabilities, and cooling effects have also been completed. Specifically, methods developed for measuring IV characteristics, PDE, and gain uniformity have become standard SiPM testing procedures for the GlueX collaboration. Valuable feedback to SensL, based on the research done in Regina, has helped to advance the technology of large area SiPMs.

The experimental design of SPMMicro PDE measurements presented in this thesis has been adapted and applied to quality assurance testing of scintillating fibres for BCAL production. Successful tests were completed using 4 m long fibres coupled at one end to a SPMMicro and at the other end to a calibrated PMT, with a collimated Sr-90 source used to excite the fibres. Using this setup, an absolute determination of

the number of photoelectrons reaching the end of a specific fibre was made. When the GlueX collaboration was investigating which fibres to use in BCAL production, several different types of scintillating fibres were measured in this way. The results of these tests were the cornerstone to that decision-making process. Since that time, BCAL production has begun in earnest, and this method of determining the absolute number of photoelectrons transmitted through a fibre has been adapted for fibre quality assurance tests, resulting in the use of a PMT as the primary fibre-testing detector, anchored by SPMMicro results.

As a result of SPMMicro tests, it was determined that 3-mm A20HD SPMMicro devices have better individual photoelectron resolution than 3-mm A35HD devices at room temperature; however, if cooling procedures are implemented, A35HD devices have excellent individual photoelectron detection capability. Since the completion of the cooling tests presented in this thesis, the GlueX collaboration has begun to explore cooling options for the BCAL readout. Even a temperature drop to 5 or 10°C would significantly reduce the dark rate of detectors used on the BCAL. Also, since breakdown voltage (and therefore overbias and gain) is temperature dependent, it is important to stabilize the temperature of SiPM detectors if they are used as the readout for the BCAL.

The improvements in performance from the first SensL flex-mounted and glass-mounted arrays sent to Regina, to the latest set of SPMP arrays is dramatic. The dark current has been reduced significantly from the original flex-mounted array, array packaging has become more robust and user-friendly, the need for external power supplies has been eliminated (while the option of using external power supplies has been maintained), and the signal quality has become more stable through adjustments to the electronic boards. Most notably, the gain uniformity of the SPMP arrays is on track to meet GlueX specifications for the detectors.

As of January 2010, the decision on BCAL readout has been made in favour of large area SiPMs, although specific detectors have not yet been selected. At present, the width of the pulses generated by the SensL arrays are incompatible with proposed front-end electronics, and are a concern for the GlueX collaboration; however, recently Hamamatsu, a relative newcomer to the large area SiPM world, has been developing large area SiPM arrays similar to those produced by SensL. These Hamamatsu arrays have thus far exhibited acceptable timing and PDE characteristics, with the need for small improvements in gain uniformity.

Moving into the future, researchers in the GlueX collaboration will continue to test SiPM detectors from both Hamamatsu and SensL until a final readout option is chosen. Now that testing methods have been established for parameters such as IV characteristics, PDE, and gain uniformity, researchers can not only continue to make these measurements of SiPM detectors, but can also focus on other parameters such as resistance to radiation. An estimate of the lifetime of these new devices is now necessary since the rapid development of large area SiPM array technology has brought the GlueX collaboration to the point where SiPMs are a realistic solution for the BCAL readout.

Finally, the research presented in this thesis on an emerging technology with great potential for particle physics, medical imaging and homeland security applications provided valuable input to SensL that resulted in the rapid maturation of large area silicon photomultiplier technology.



# References

- [1] Jack Paton. The Flux Tube Model. *Nuclear Physics*, A446:419–423, 1985.
- [2] M. Gell-Mann. A Schematic Model of Baryons and Mesons. *Physics Letters*, 8(3):214 – 215, 1964.
- [3] V. Crede and C.A. Meyer. The Experimental Status of Glueballs. *Progress in Particle and Nuclear Physics*, 63(1):74 – 116, 2009.
- [4] A. R. Dzierba et al. The Search for QCD Exotics. *American Scientist*, 88(5):406, 2000.
- [5] G. Koleva. Beam Tests for the GlueX Barrel Calorimeter Prototype. Master’s thesis, University of Regina, 2006. GlueX-doc-824-v1.
- [6] C. Meyer. GlueX Physics and Detector Performance Metrics. Technical report, GlueX Collaboration, 2008. GlueX-doc-999-v9.
- [7] C. Meyer. Potential GlueX Physics During the First Two Years of 12 GeV Running. Technical report, GlueX Collaboration, 2006. GlueX-doc-621-v2.
- [8] Z. Papandreou. The Gluex Project at Jefferson Lab. Int. Conf. on Hadron Spectroscopy, October 2007. Frascati Physics Series Vol. XLVI.
- [9] J. J. Sakurai. Vector-meson dominance and high-energy electron-proton inelastic scattering. *Phys. Rev. Lett.*, 22(18):981–984, May 1969.

- [10] J. Kuhn and C. Meyer. Acceptance Study for the GlueX detector system. Technical report, GlueX Collaboration, 2004. GlueX-doc-264-v2.
- [11] A. Dzierba et al. BCAL: The Barrel Calorimeter. Technical report, GlueX Collaboration, 2008. GlueX-doc-986-v3.
- [12] D. Lawrence. The GlueX Detector. Technical report, GlueX Collaboration, 2009. GlueX-doc-1292-v7.
- [13] E. S. Smith. Design goals for the Hall D detector and subsystems. Technical report, GlueX Collaboration, 2008. GlueX-doc-866-v10.
- [14] M. Adinolfi et al. The KLOE electromagnetic calorimeter. *Nucl. Instr. and Meth. A*, 482(1-2):364 – 386, 2002.
- [15] B.D. Leverington et al. Performance of the prototype module of the GlueX electromagnetic barrel calorimeter. *Nucl. Instr. and Meth. A*, 596(3):327 – 337, 2008.
- [16] A. Semenov et al. Analysis of Amplitude Information from 2006 BCAL Cosmics Runs. Technical report, GlueX Collaboration, 2007. GlueX-doc-845-v4.
- [17] Z. Papandreou. BCAL Overview for Readout Review. Technical report, GlueX Collaboration, 2009. GlueX-doc-1308-v2.
- [18] St. Gobain Crystals Scintillating Optical Fibers. Brochure 605.
- [19] T. Förster. Transfer Mechanisms of Electronic Excitation. *Discussions of the Faraday Society*, 27:7, 1959.
- [20] A. Pla-Dalmau. 2-(2'-Hydroxyphenyl) benzothiazoles, -benzoxazoles, and -benzimidazoles for Plastic Scintillation Applications. *Journal of Organic Chemistry*, 60:5468–5473, 1995.

- [21] N. Kolev et al. Dependence of the Spatial and Energy Resolution of BCAL on Segmentation. Technical report, GlueX Document, 2007. GlueX-doc-659-v2.
- [22] W. Boeglin. Report on FM PMT properties for the BCAL readout review. Technical report, GlueX Collaboration, 2009. GlueX-doc-1311-v4.
- [23] P. Ioannou et al. BCAL readout utilizing field-resistant PMT's. Technical report, GlueX Collaboration, 2006. GlueX-doc-712-v2.
- [24] A. Gasanov, V. Golovin, Z. Sadygov, and N. Yusipov. Avalanche optical detector, October 1989. European Patent No. SU1702831.
- [25] G. Bondarenko et al. Limited Geiger-mode Microcell Silicon Photodiode: New Results. *Nucl. Instr. and Meth. A*, 442(1-3):187 – 192, 2000.
- [26] P. Buzhan et al. Silicon photomultiplier and its possible applications. *Nucl. Instr. and Meth. A*, 504(1-3):48 – 52, 2003. Proceedings of the 3rd International Conference on New Developments in Photodetection.
- [27] Z. Papandreou. Silicon Photomultiplier Primer. Technical report, GlueX Collaboration, 2007. GlueX-doc-741-v2.
- [28] F. Zappa et al. Principles and Features of Single-photon Avalanche Diode Arrays. *Sensors and Actuators A: Physical*, 140(1):103 – 112, 2007.
- [29] E. H. S. Burhop. The Auger Effect. *Proceedings of the Royal Society of London. Series A, Mathematical and Physical Sciences*, 148(864):272–284, 1935.
- [30] W. Shockley and W. T. Read. Statistics of the recombinations of holes and electrons. *Phys. Rev.*, 87(5):835–842, Sep 1952.
- [31] SensL SPM Technical and Application Notes, 2007. Electronic document. 2007.

- [32] B. Leverington. Light Guide Design for Phase 1 GlueX Sensor Module R & D. Technical report, GlueX Collaboration, 2006. GlueX-doc-651-v1.
- [33] Z. Papandreou, B. Leverington, and G. Lolos. Spectral response of scintillating fibers. *Nucl. Instrum. Meth.*, A596:338–346, 2008.